

Supporting Information

A Rolling-mode Triboelectric Nanogenerator with Multi-tunnel Grating Electrodes and Opposite-charge-enhancement for Wave Energy Harvesting

Yawei Wang^{1,2, ‡}, Hengxu Du^{2, ‡}, Hengyi Yang^{2, ‡}, Ziyue Xi^{2, ‡}, Cong Zhao², Zian Qian², Xinyuan Chuai³, Xuzhang Peng¹, Hongyong Yu², Yu Zhang², Xin, Li³, Guobiao Hu^{1, *}, Hao Wang^{2, *}, Minyi Xu^{2, *}

¹*Internet of Things, Thrust, The Hong Kong University of Science and Technology (Guangzhou), Nansha, Guangzhou 511400, China*

²*Dalian Key Lab of Marine Micro/Nano Energy and Self-powered Systems, Marine Engineering College, Dalian Maritime University, Dalian 116026, China*

³*Advanced Manufacturing Technology Innovation Center, Xidian University, Guangzhou 510555, China*

[‡] *These authors contributed equally to this work*

^{*} *Correspondence:* guobiaohu@hkust-gz.edu.cn (GH); hao8901@dlmu.edu.cn (HW); xuminyi@dlmu.edu.cn (MX)

Table of Contents

Figure S1: Photographs of the F-TENG (a-b) and the M-TENG (c-d).	5
Figure S2: Comparison of the transferred charges in the F-TENG and M-TENG.....	6
Figure S3: Contact electrification between two different dielectrics. (a) Before contact, due to their different valence and conduction band structures, Nylon's occupied surface states possess higher energy than PTFE's unoccupied surface states. (b) In contact, some electrons transfer from the Nylon's surface to the PTFE's surface, leading to contact electrification. (c) After contact, positive and negative electrostatic charges stay on Nylon's and PTFE's surfaces, respectively. These charges are indefinitely stable under undisturbed conditions. However, thermal fluctuations and elevated temperatures can cause these electrons to be released from their surface states.....	7
Figure S4: Working principle of a single TENG unit using Nylon balls (a), PTFE balls (b), and both of them (c).....	8
Figure S5: Electric potential distributions of MO-TENGs with two dielectric balls at different positions simulated using COMSOL Multiphysics software.....	9
Figure S6: Electric potential distributions of MO-TENGs with six dielectric balls at different positions simulated using COMSOL Multiphysics software.....	10
Figure S7: Photograph of the assembled MO-TENG.....	11
Figure S8: Dimension details of the MO-TENG in the perspective view (a), X-Y view (b), X-Z view (c), and zoomed-in view (d).....	12
Figure S9: Step-by-step fabrication tutorial of the MO-TENG.....	13
Figure S10: Illustration of the linear motor test bench designed for generating desired external excitations in the experiment.	14
Figure S11: The photograph of the linear motor test bench used in the experiment for generating desired external excitations.....	15
Figure S12: Detailed view of charge transfer accumulation process depicted in Figure 3e, with time intervals from 0 to 3.5 seconds (a), 10 to 13.5 seconds (b), and 259.1 to 262.2 seconds (c).	16
Figure S13: Comparison of V_{oc} (a), I_{sc} (b), Q_{sc} (c), and rectified charge (d) generated by the M-TENG and MO-TENG.....	17
Figure S14: Measurement of the capacitance of the M-TENG (a) and the MO-TENG (b).....	18
Figure S15: Peak values of the voltage (a) and current (b) signals produced by the MO-TENG in one cycle.....	19
Figure S16: Photograph of the swing test bench.	20
Figure S17: Voltage output responses produced by the MO-TENG under various excitation angles: (a) $\theta = 5^\circ$, (b) $\theta = 10^\circ$, (c) $\theta = 15^\circ$, (d) $\theta = 20^\circ$, (e) $\theta = 25^\circ$, (f) $\theta = 30^\circ$	21
Figure S18: Time-history current responses and the corresponding RMS values produced by the MO-TENG under various excitation angles: (a) $\theta = 5^\circ$, (b) $\theta = 10^\circ$, (c) $\theta = 15^\circ$, (d) $\theta = 20^\circ$, (e) $\theta = 25^\circ$, (f) $\theta = 30^\circ$	22

Figure S19: Transfer charge responses of the MO-TENG under various excitation angles: (a) $\theta = 5^\circ$, (b) $\theta = 10^\circ$, (c) $\theta = 15^\circ$, (d) $\theta = 20^\circ$, (e) $\theta = 25^\circ$, (f) $\theta = 30^\circ$	23
Figure S20: Voltage responses of the MO-TENG under various excitation frequencies: (a) $f = 0.1$ Hz, (b) $f = 0.2$ Hz, (c) $f = 0.3$ Hz, (d) $f = 0.4$ Hz, (e) $f = 0.5$ Hz.....	24
Figure S21: Time-history current responses and the corresponding RMS values produced by the MO-TENG under various excitation frequencies: (a) $f = 0.1$ Hz, (b) $f = 0.2$ Hz, (c) $f = 0.3$ Hz, (d) $f = 0.4$ Hz, (e) $f = 0.5$ Hz.....	25
Figure S22: Transfer charge of the MO-TENG under various excitation frequencies: (a) $f = 0.1$ Hz, (b) $f = 0.2$ Hz, (c) $f = 0.3$ Hz, (d) $f = 0.4$ Hz, (e) $f = 0.5$ Hz.....	26
Figure S23: Load resistance-dependence of the peak power and generated current produced by the MO-TENG (a) and the M-TENG (b).....	27
Figure S24: Load resistance-dependence of the RMS power and RMS current produced by the MO-TENG (a) and the M-TENG (b).....	28
Figure S25: Comparison of the peak and RMS power densities in this work with others ¹⁻⁸	29
Figure S26: Peak power outputs of a stacked MO-TENG with 10 units excited by a 6-degree-of-freedom platform (a) and in the wave tank (b).....	30
Figure S27: RMS power outputs of a stacked MO-TENG with 10 units excited by a 6-degree-of-freedom platform (a) and in the wave tank (b).....	31
Figure S28: Photograph of the three-degree-of-freedom (3-DOF) swing platform.	32
Figure S29: Photograph of the regular wave tank.	33
Figure S30: The charging histories of a single MO-TENG using PMM for different capacitors.	34
Figure S31: Powering marine navigation light with stacked MO-TENGs in the water tank.....	35
Figure S32: The schematic diagram of the angle α between the tunnel orientation and the wave direction.	36
Figure S33: The current output and transfer charge of stacked 10 MO-TENG units with different α . Data are presented as mean values \pm SD.	37
Figure S34: Dimension details of the acrylic buoy shown in Figure 4h-i.	38
Figure S35: Photograph of the buoy stacked with 30 MO-TENG units.....	39
Figure S36: Photograph of the random wave tank.	40
Figure S37: Photograph of the stacked MO-TENGs executing sensing tasks in the real ocean environment.	41
Table S1. Summary of previously reported TENGs for blue energy harvesting.	42
Supplementary Note 1. The diameter selection of dielectric balls and multi-tunnel grating electrodes	45
Figure N1: Photograph of rolling mode TENGs fabricated using PTFE balls with different diameters.	46
Figure N2: The parameter illustration of rolling mode TENGs fabricated using PTFE balls with different diameters.....	46

Figure N3: The weight, transfer charge, and charge weight densities of rolling mode TENGs using PTFE balls of various diameters. Data are presented as mean values ± SD.....	46
Figure N4: The transfer charge of rolling mode TENGs fabricated with one tunnel and 4 segment electrodes of various tunnel diameters.....	47
Figure N5: The current output of one tunnel grating electrode TENGs with different electrode segments.....	47
Supplementary Note 2. The parameters of the designed buoy	48
Figure N6: The selection of buoy diameter based on RAO.....	48
Figure N7: The selection of buoy vertical CoG based on RAO.....	49
Supplementary Movie 1. MO-TENGs for lighting up LEDs.....	50
Supplementary Movie 2. MO-TENGs for self-powered water quality sensing.....	50
Supplementary Movie 3. MO-TENGs for powering marine navigation light.....	50
Supplementary Movie 4. MO-TENGs enabled self-powered sensing under wave excitation.....	50
Supplementary Movie 5. MO-TENGs enabled self-powered sensing in random wave tank.....	50
Supplementary Movie 6. MO-TENGs enabled self-powered sensing in real ocean environment.....	50
Reference	51

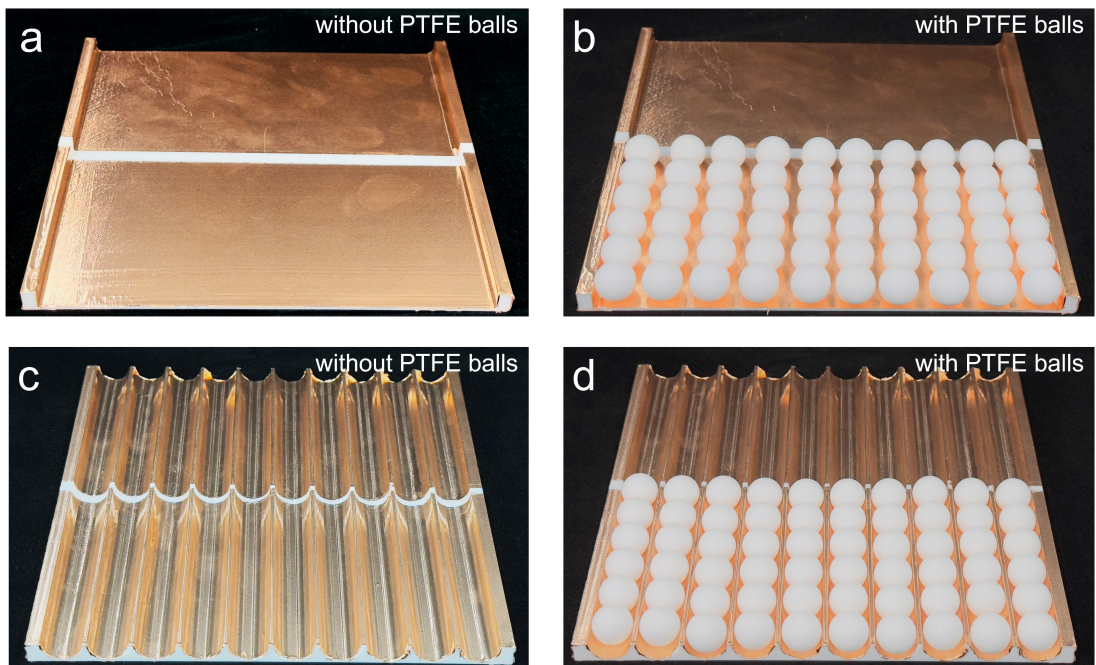


Figure S1: Photographs of the F-TENG (a-b) and the M-TENG (c-d).

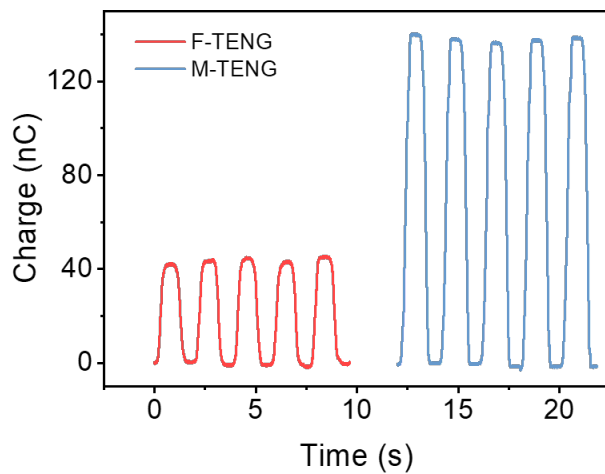


Figure S2: Comparison of the transferred charges in the F-TENG and M-TENG.

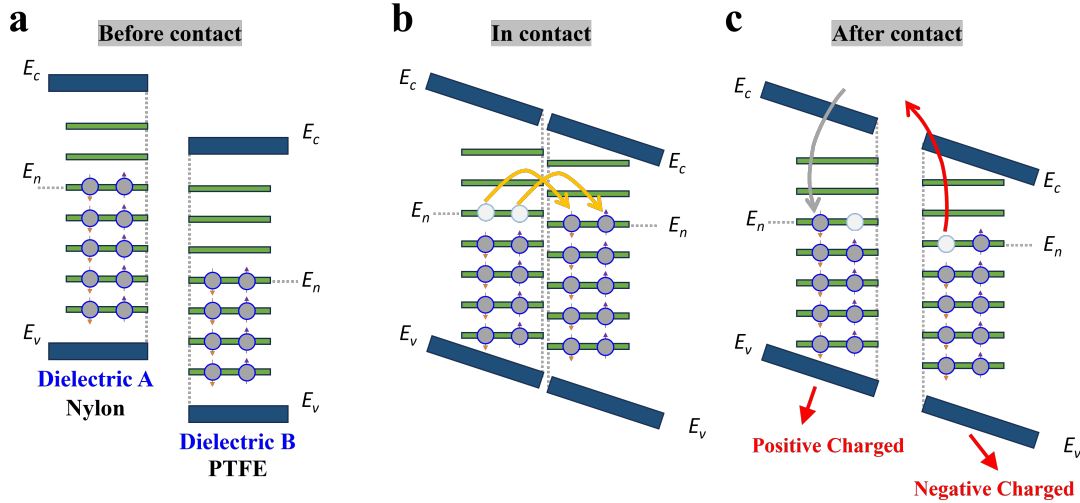


Figure S3: Contact electrification between two different dielectrics. (a) Before contact, due to their different valence and conduction band structures, Nylon's occupied surface states possess higher energy than PTFE's unoccupied surface states. (b) In contact, some electrons transfer from the Nylon's surface to the PTFE's surface, leading to contact electrification. (c) After contact, positive and negative electrostatic charges stay on Nylon's and PTFE's surfaces, respectively. These charges are indefinitely stable under undisturbed conditions. However, thermal fluctuations and elevated temperatures can cause these electrons to be released from their surface states.

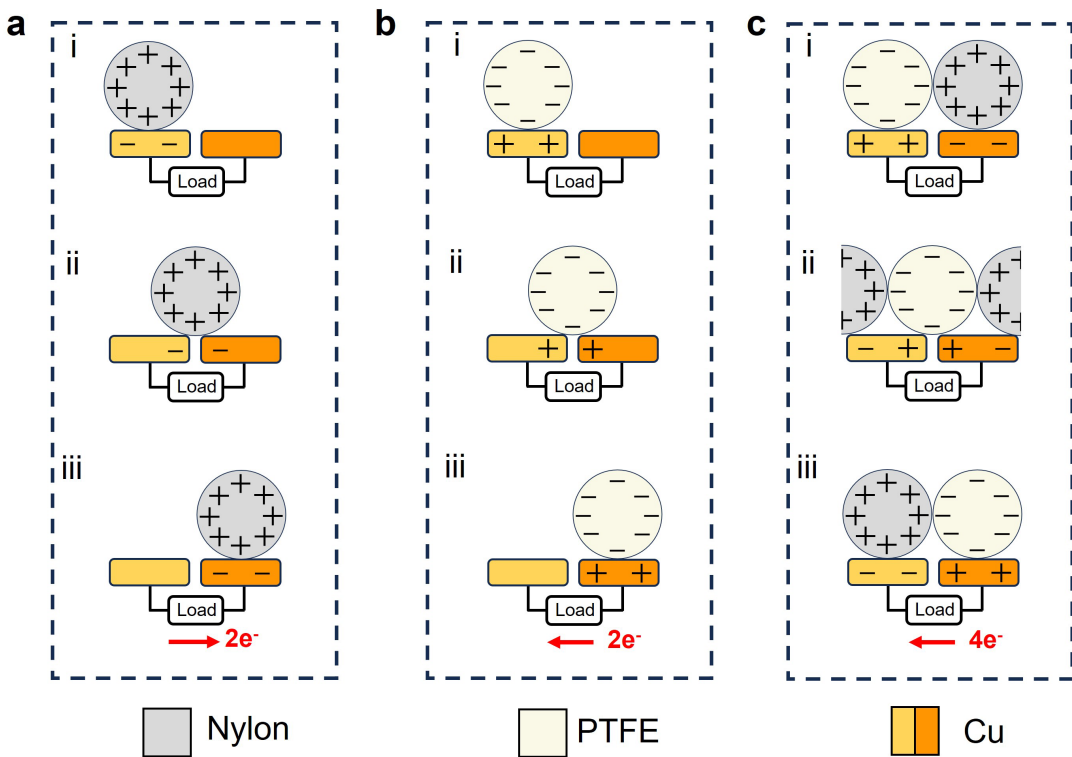


Figure S4: Working principle of a single TENG unit using Nylon balls (a), PTFE balls (b), and both of them (c).

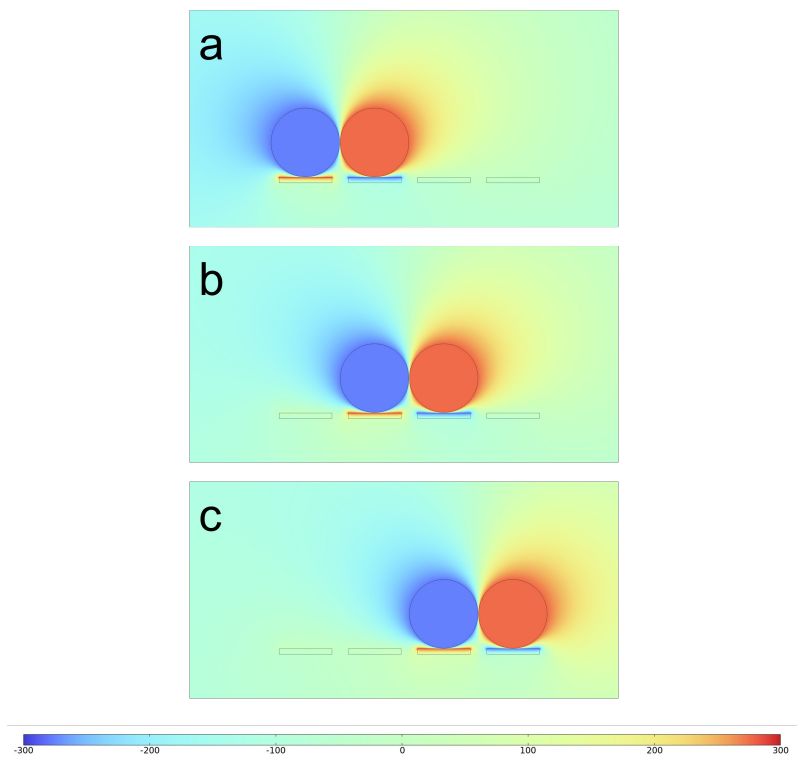


Figure S5: Electric potential distributions of MO-TENGs with two dielectric balls at different positions simulated using COMSOL Multiphysics software.

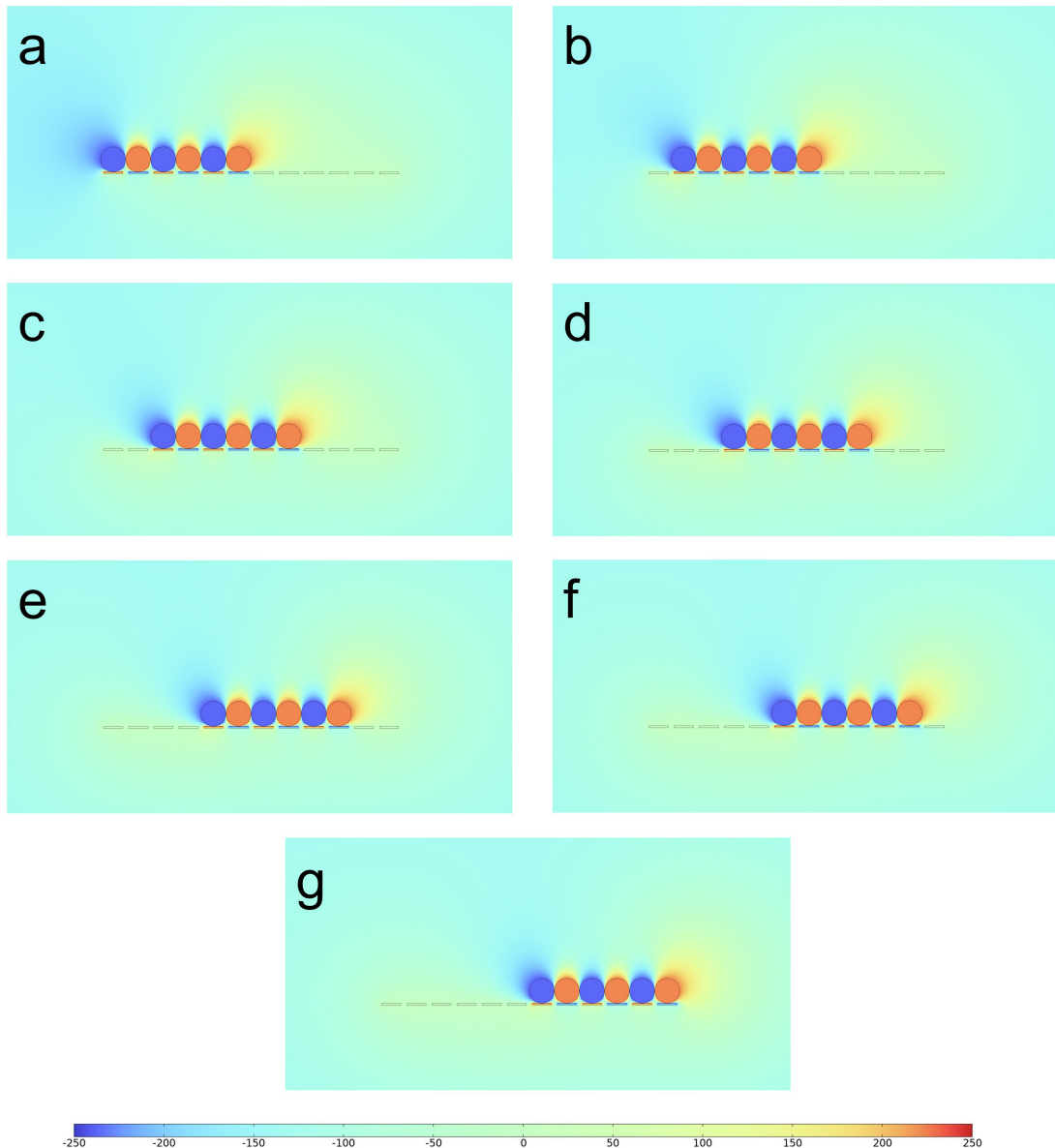


Figure S6: Electric potential distributions of MO-TENGs with six dielectric balls at different positions simulated using COMSOL Multiphysics software.

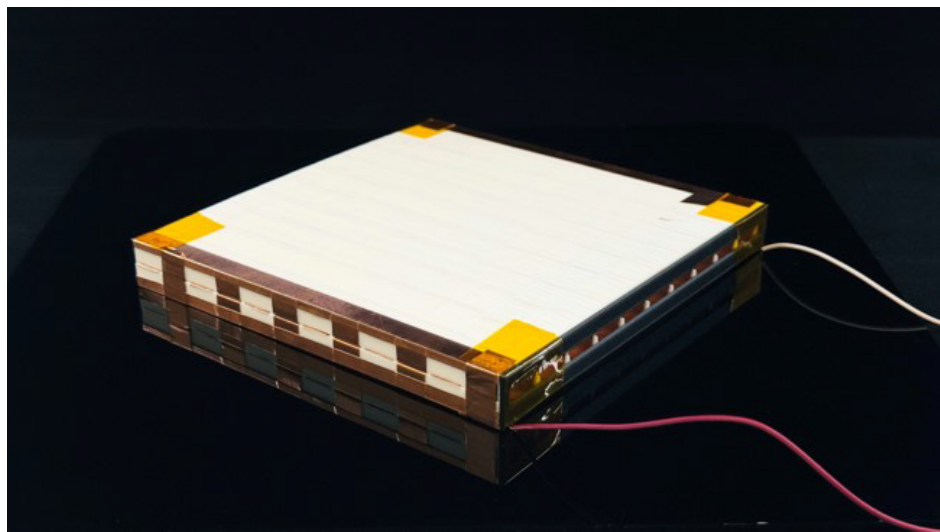


Figure S7: Photograph of the assembled MO-TENG.

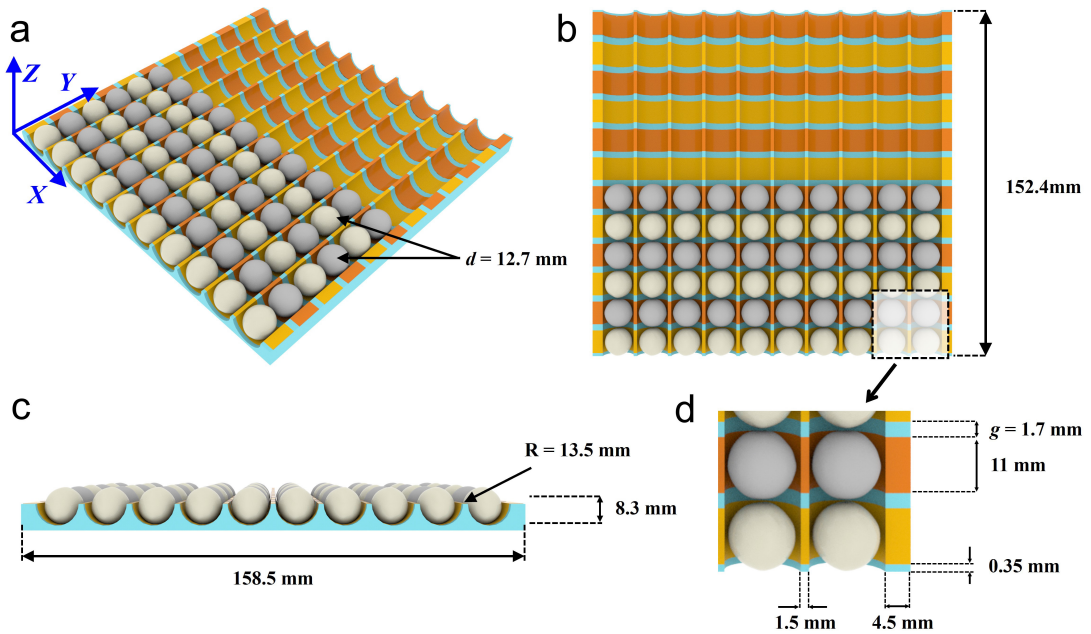


Figure S8: Dimension details of the MO-TENG in the perspective view (a), X-Y view (b), X-Z view (c), and zoomed-in view (d).

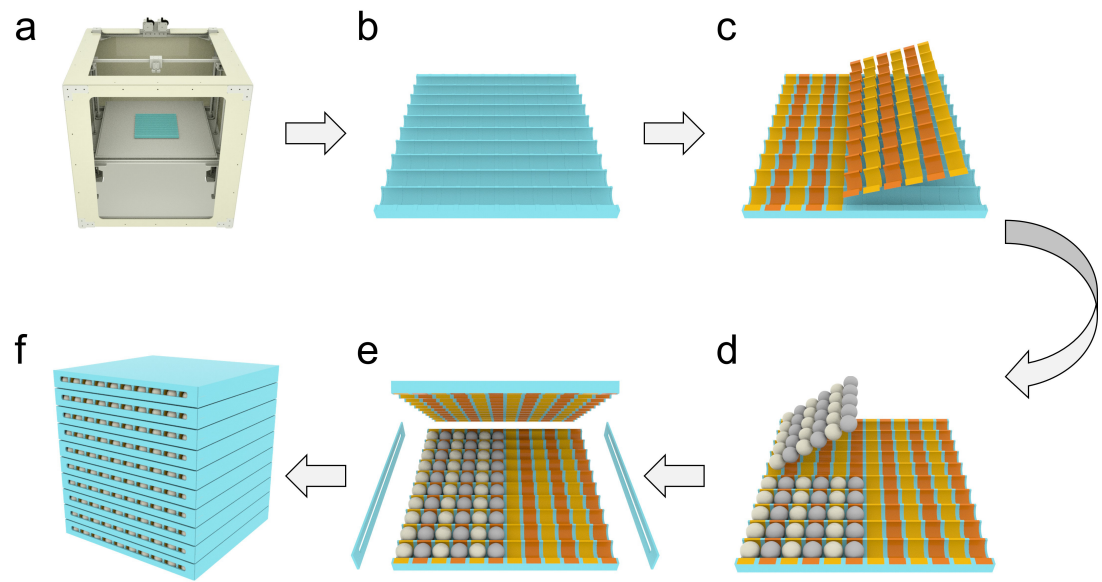


Figure S9: Step-by-step fabrication tutorial of the MO-TENG.

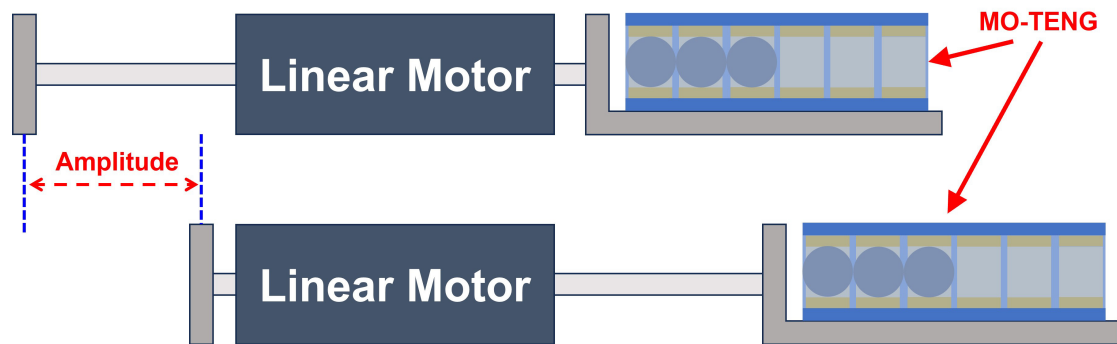


Figure S10: Illustration of the linear motor test bench designed for generating desired external excitations in the experiment.

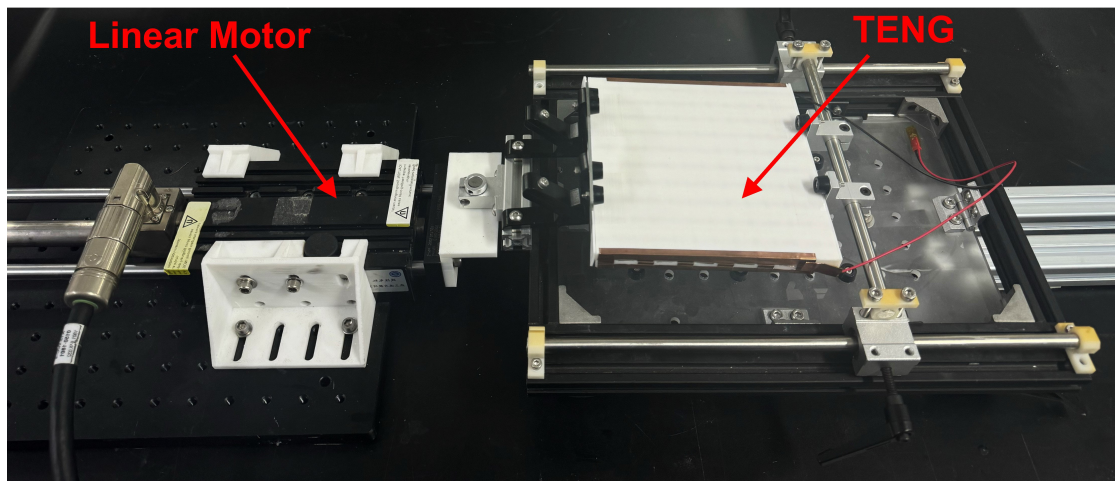


Figure S11: The photograph of the linear motor test bench used in the experiment for generating desired external excitations.

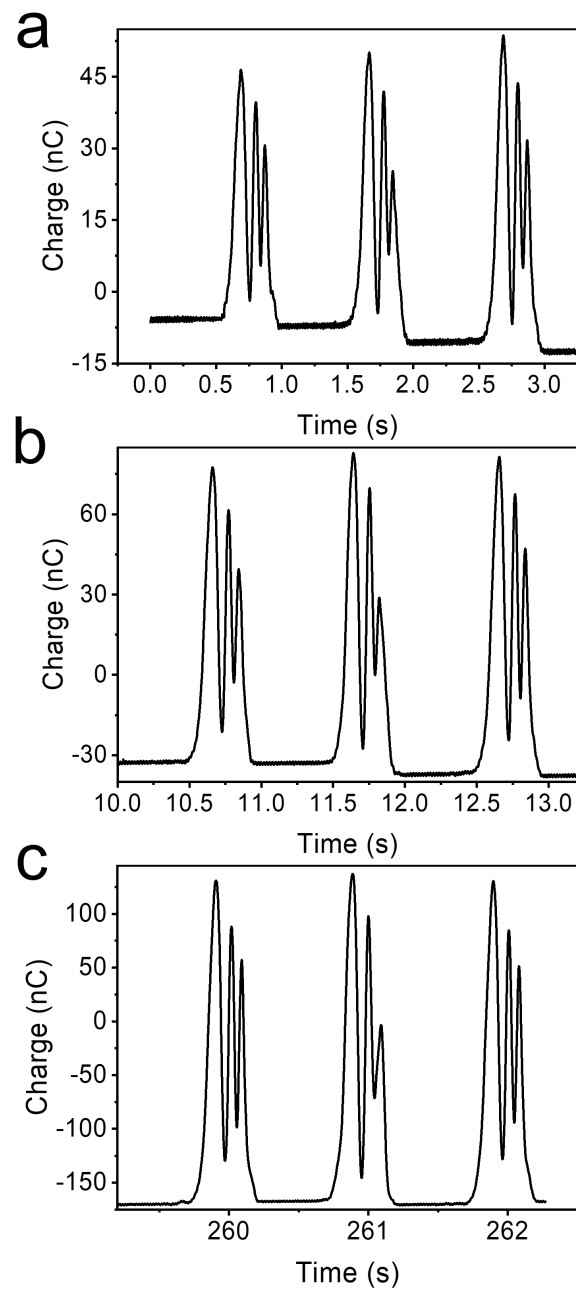


Figure S12: Detailed view of charge transfer accumulation process depicted in Figure 3e, with time intervals from 0 to 3.5 seconds (a), 10 to 13.5 seconds (b), and 259.1 to 262.2 seconds (c).

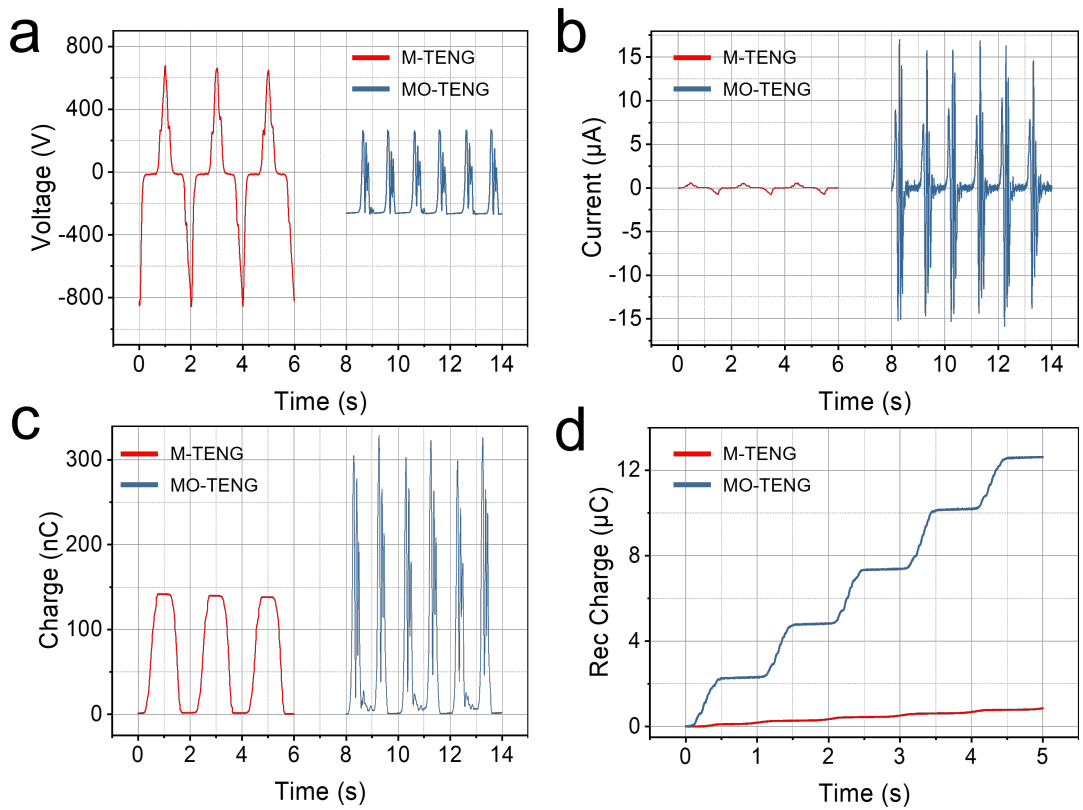


Figure S13: Comparison of V_{oc} (a), I_{sc} (b), Q_{sc} (c), and rectified charge (d) generated by the M-TENG and MO-TENG.

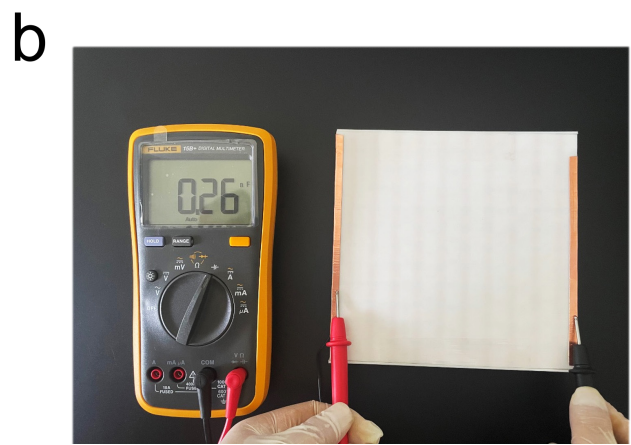
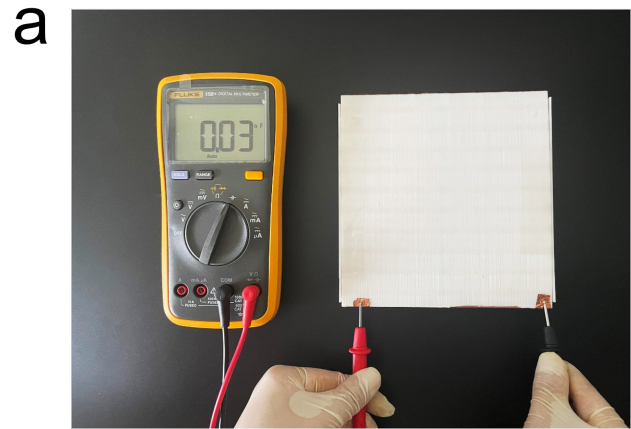


Figure S14: Measurement of the capacitance of the M-TENG (a) and the MO-TENG (b).

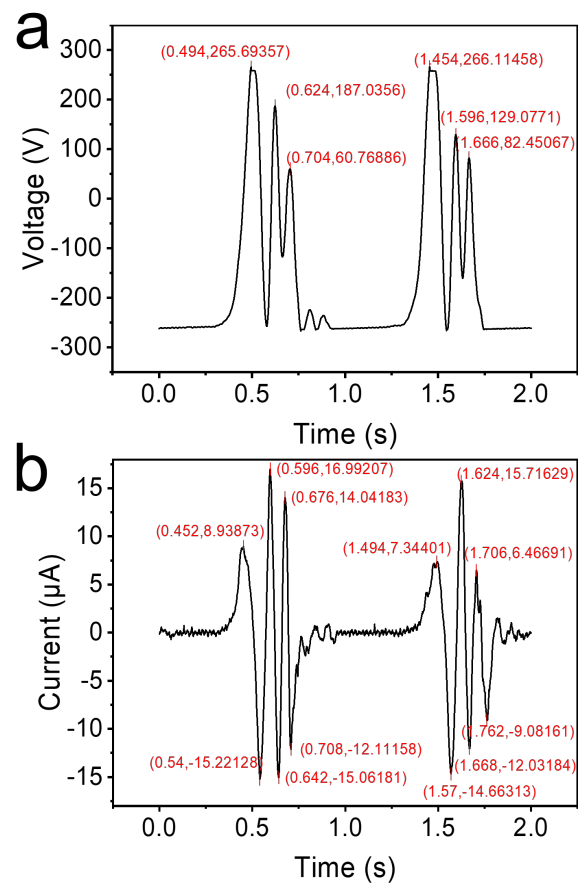


Figure S15: Peak values of the voltage (a) and current (b) signals produced by the MO-TENG in one cycle.

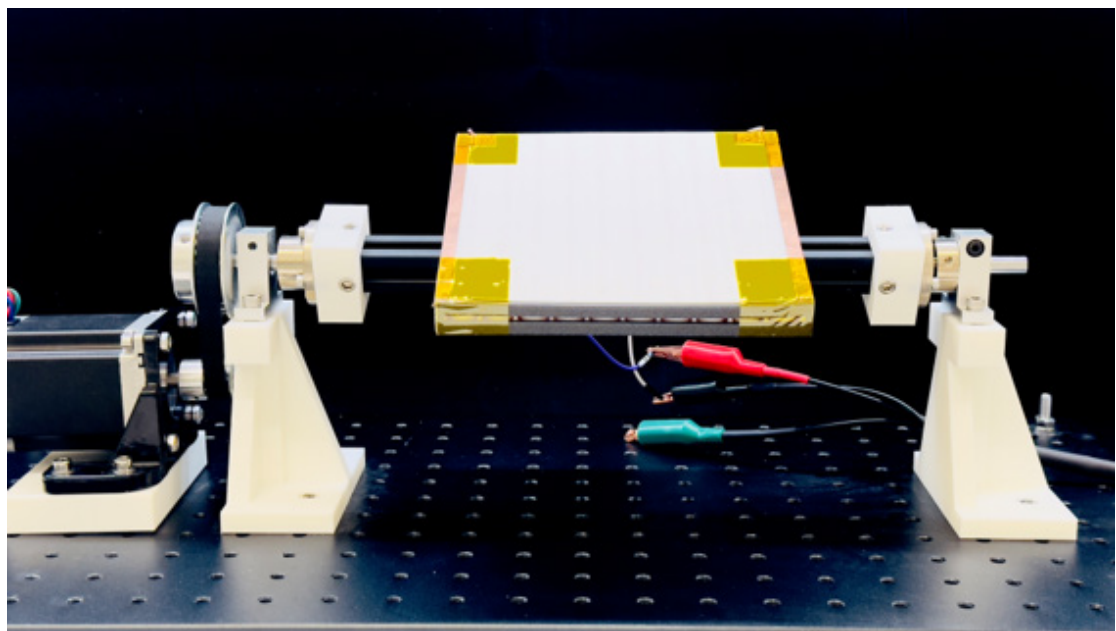


Figure S16: Photograph of the swing test bench.

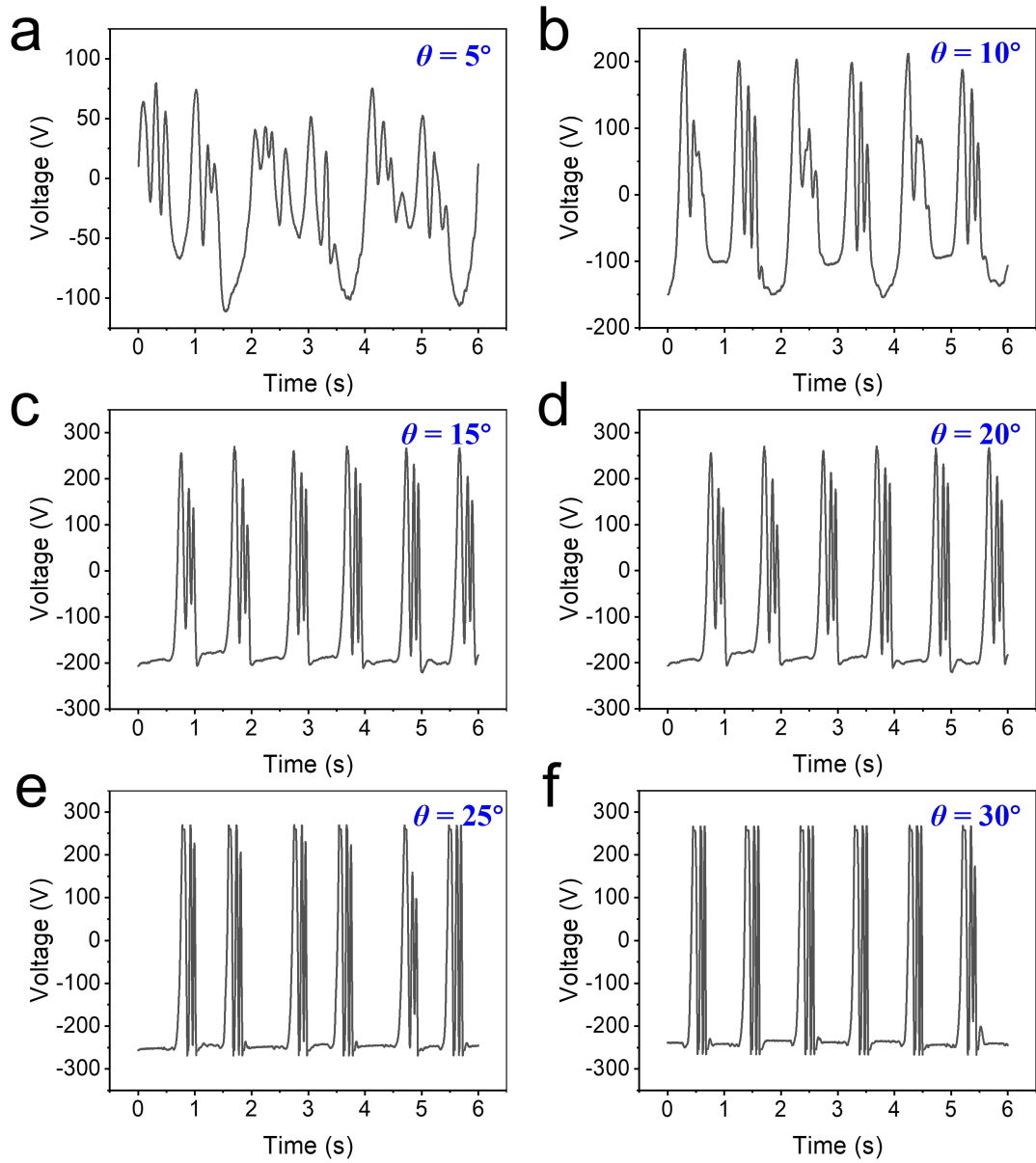


Figure S17: Voltage output responses produced by the MO-TENG under various excitation angles: (a) $\theta = 5^\circ$, (b) $\theta = 10^\circ$, (c) $\theta = 15^\circ$, (d) $\theta = 20^\circ$, (e) $\theta = 25^\circ$, (f) $\theta = 30^\circ$.

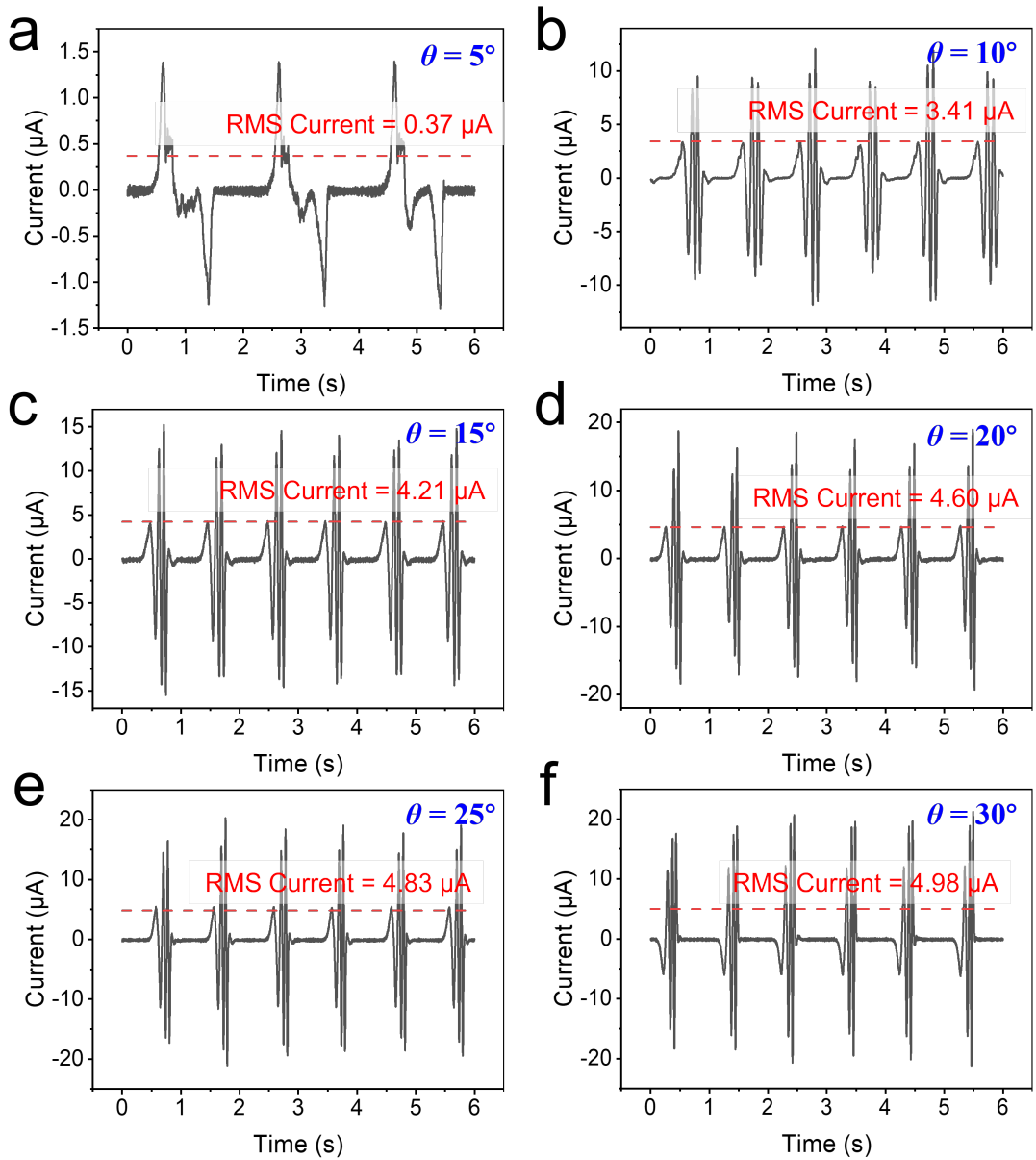


Figure S18: Time-history current responses and the corresponding RMS values produced by the MO-TENG under various excitation angles: (a) $\theta = 5^\circ$, (b) $\theta = 10^\circ$, (c) $\theta = 15^\circ$, (d) $\theta = 20^\circ$, (e) $\theta = 25^\circ$, (f) $\theta = 30^\circ$.

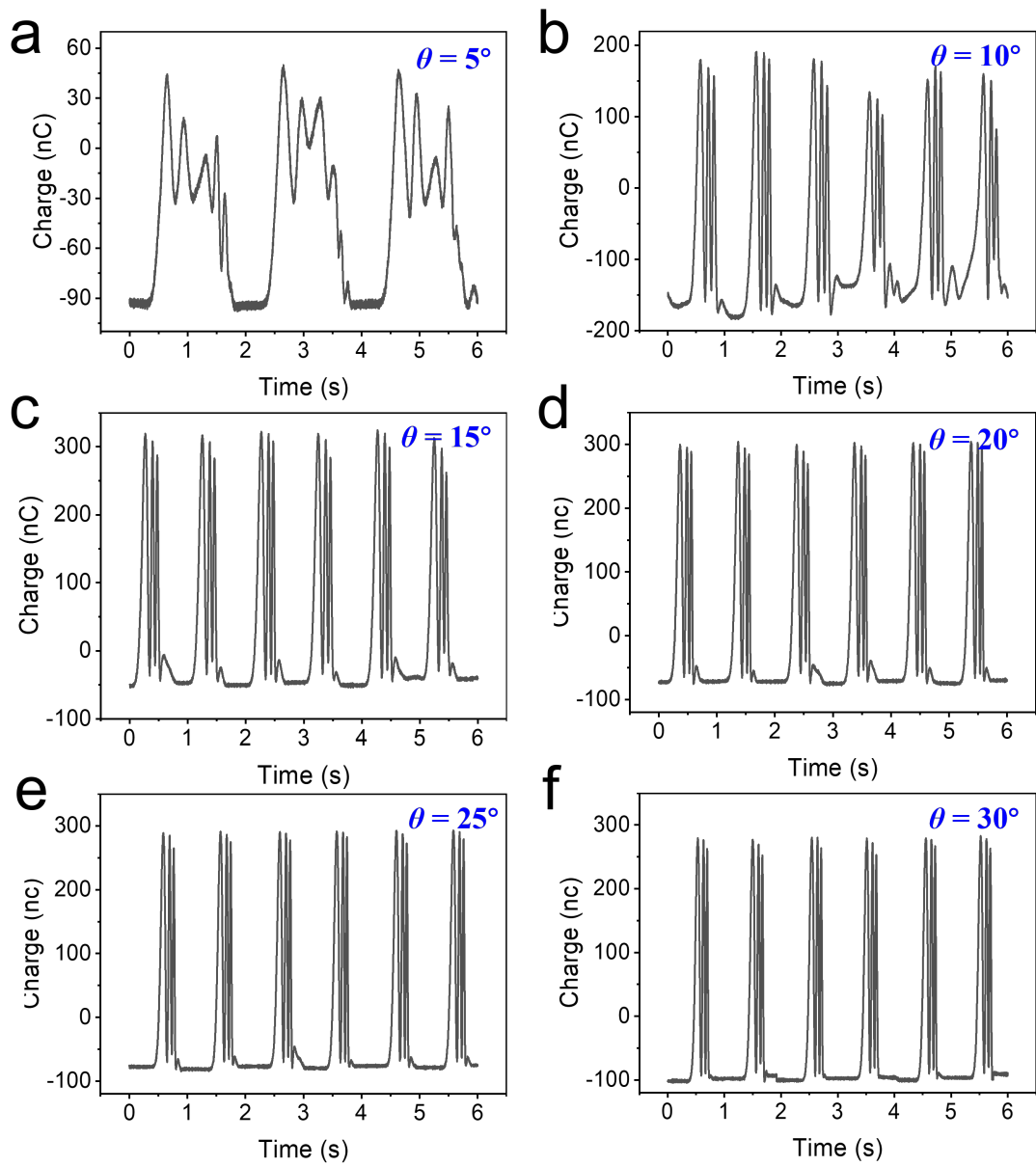


Figure S19: Transfer charge responses of the MO-TENG under various excitation angles: (a) $\theta = 5^\circ$, (b) $\theta = 10^\circ$, (c) $\theta = 15^\circ$, (d) $\theta = 20^\circ$, (e) $\theta = 25^\circ$, (f) $\theta = 30^\circ$.

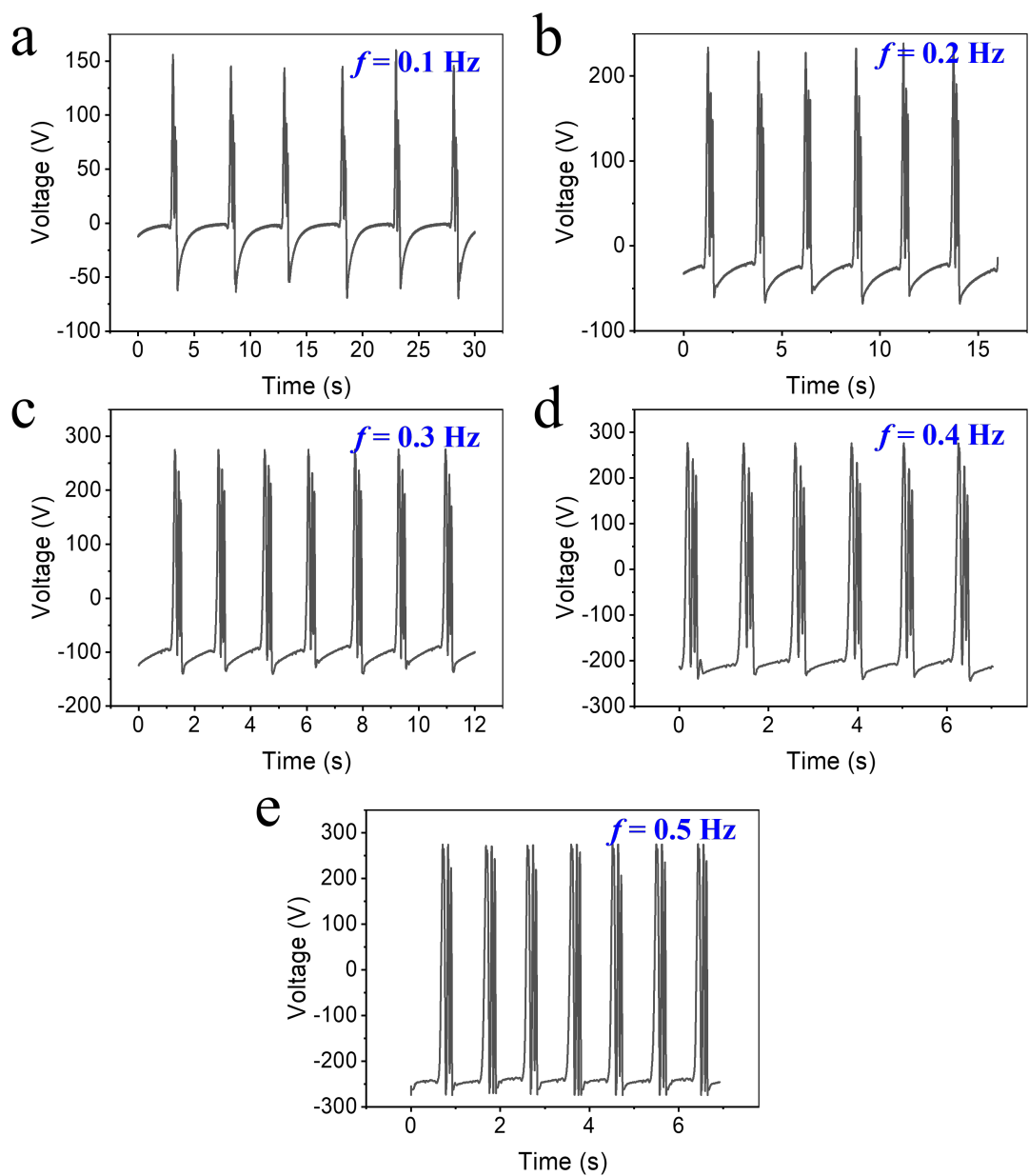


Figure S20: Voltage responses of the MO-TENG under various excitation frequencies:
 (a) $f = 0.1 \text{ Hz}$, (b) $f = 0.2 \text{ Hz}$, (c) $f = 0.3 \text{ Hz}$, (d) $f = 0.4 \text{ Hz}$, (e) $f = 0.5 \text{ Hz}$.

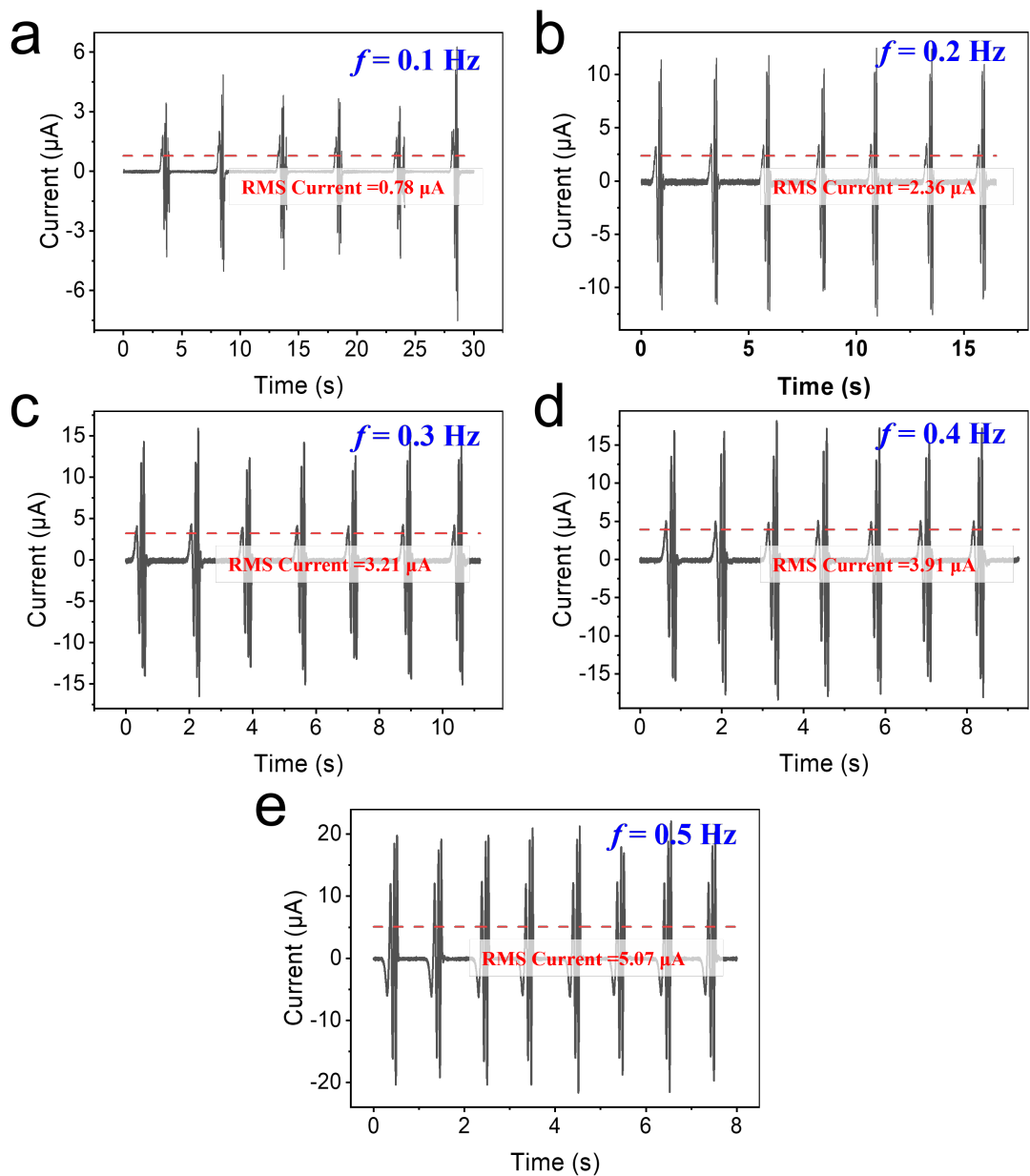


Figure S21: Time-history current responses and the corresponding RMS values produced by the MO-TENG under various excitation frequencies: (a) $f = 0.1 \text{ Hz}$, (b) $f = 0.2 \text{ Hz}$, (c) $f = 0.3 \text{ Hz}$, (d) $f = 0.4 \text{ Hz}$, (e) $f = 0.5 \text{ Hz}$.

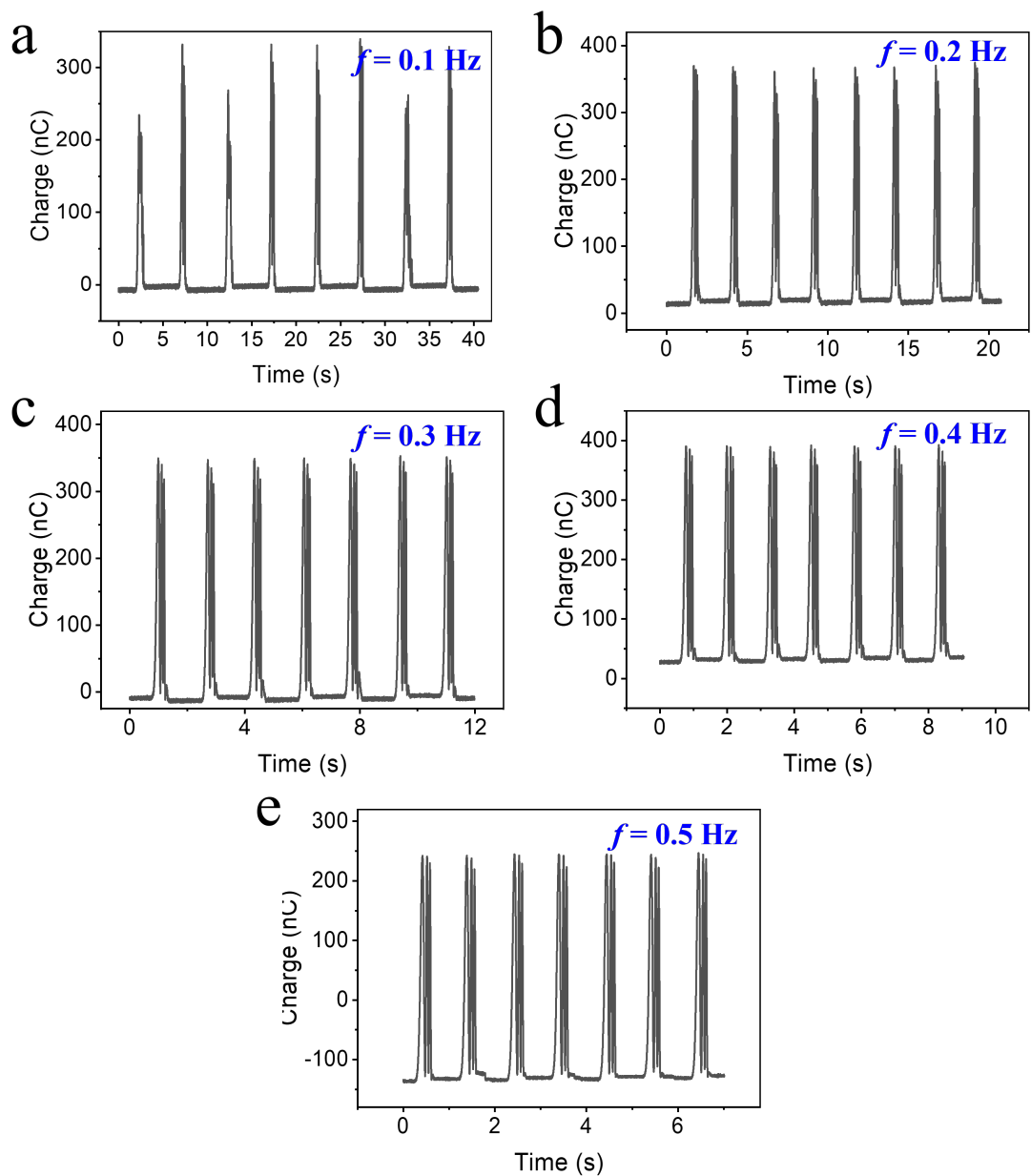


Figure S22: Transfer charge of the MO-TENG under various excitation frequencies:
 (a) $f = 0.1 \text{ Hz}$, (b) $f = 0.2 \text{ Hz}$, (c) $f = 0.3 \text{ Hz}$, (d) $f = 0.4 \text{ Hz}$, (e) $f = 0.5 \text{ Hz}$.

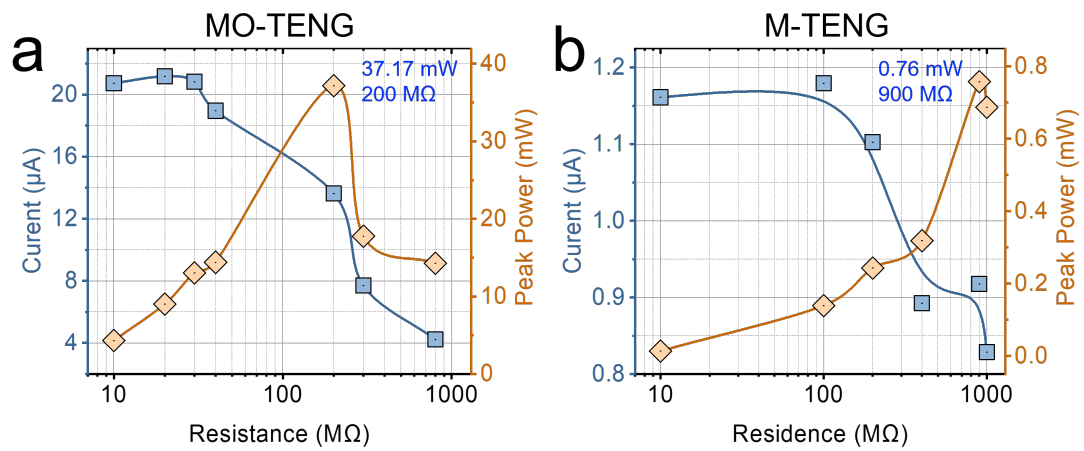


Figure S23: Load resistance-dependence of the peak power and generated current produced by the MO-TENG (a) and the M-TENG (b).

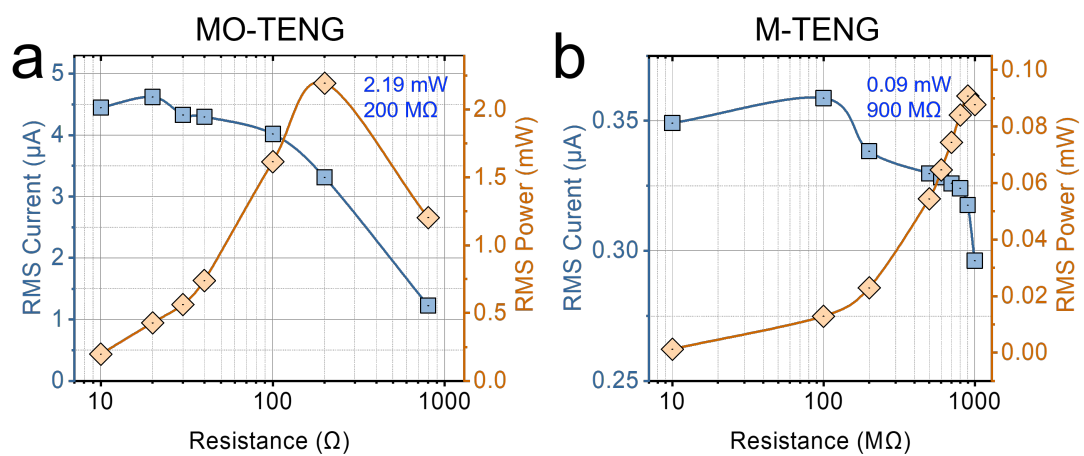


Figure S24: Load resistance-dependence of the RMS power and RMS current produced by the MO-TENG (a) and the M-TENG (b).

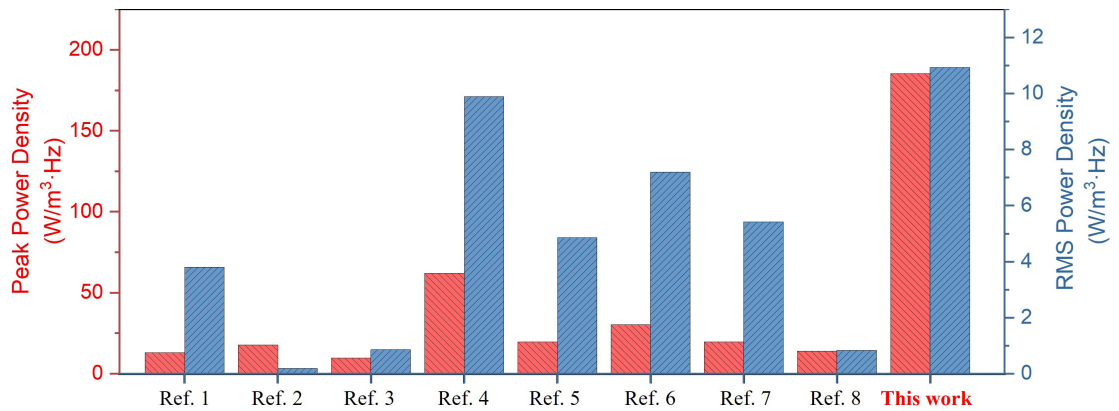


Figure S25: Comparison of the peak and RMS power densities in this work with others¹⁻⁸.

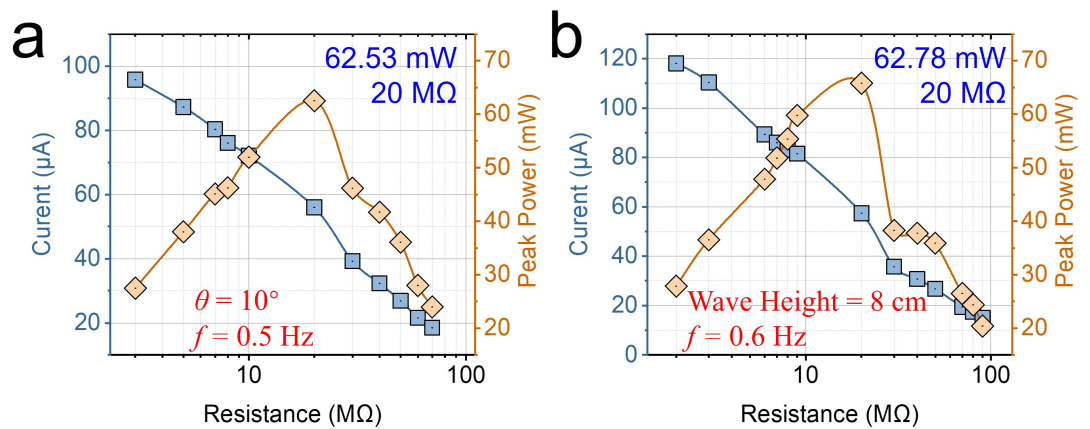


Figure S26: Peak power outputs of a stacked MO-TENG with 10 units excited by a 6-degree-of-freedom platform (a) and in the wave tank (b).

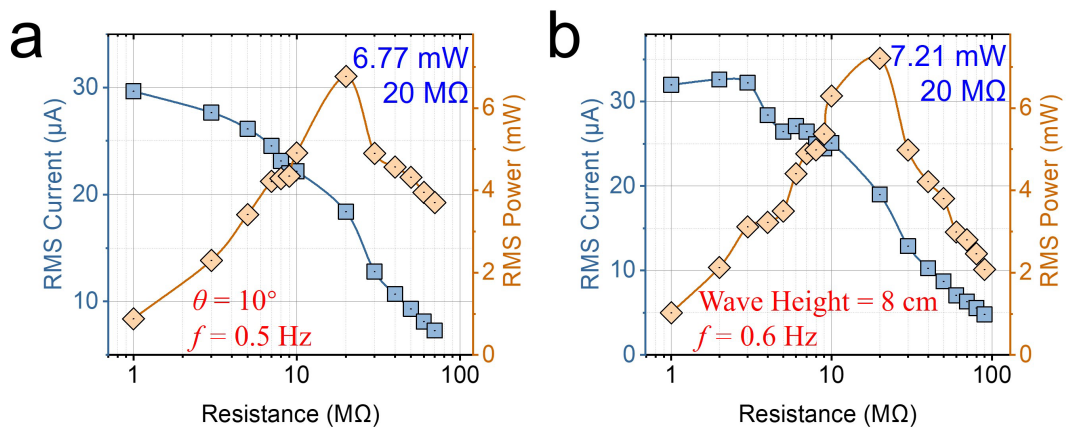


Figure S27: RMS power outputs of a stacked MO-TENG with 10 units excited by a 6-degree-of-freedom platform (a) and in the wave tank (b).

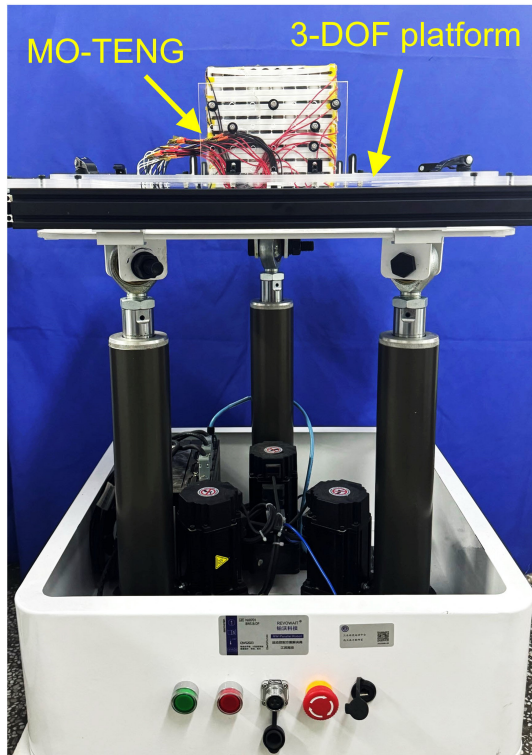


Figure S28: Photograph of the three-degree-of-freedom (3-DOF) swing platform.

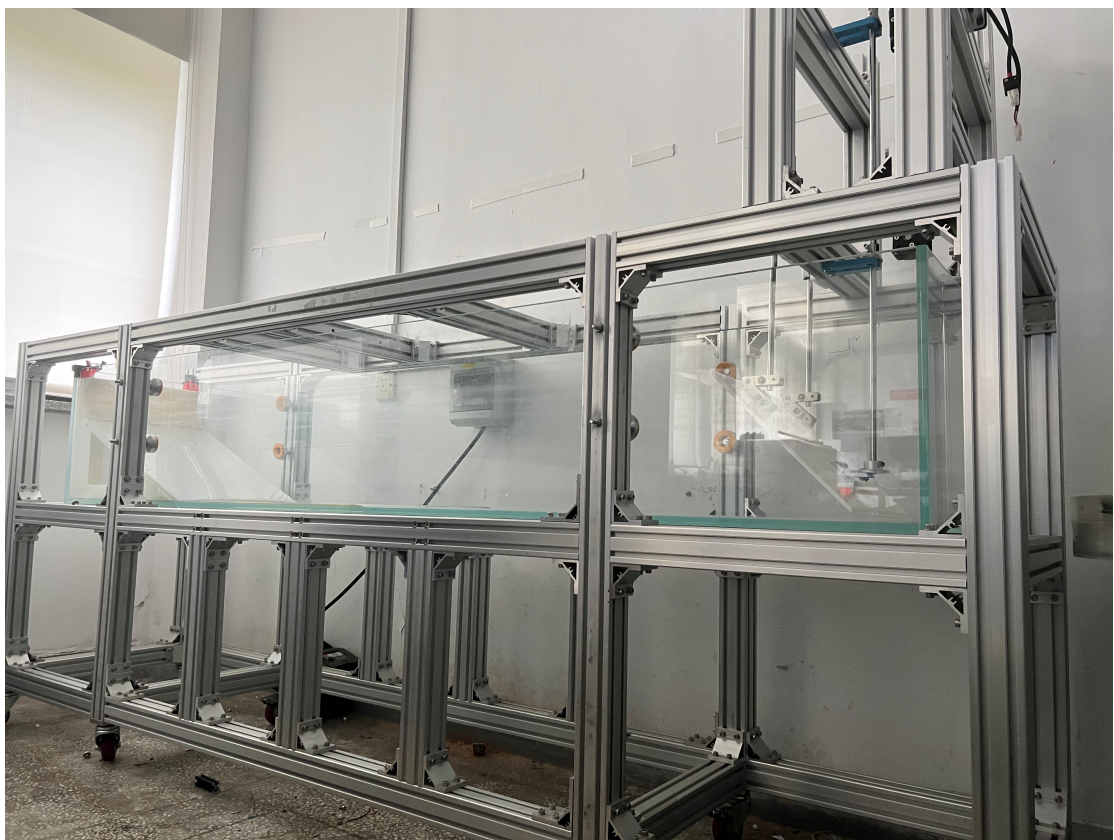


Figure S29: Photograph of the regular wave tank.

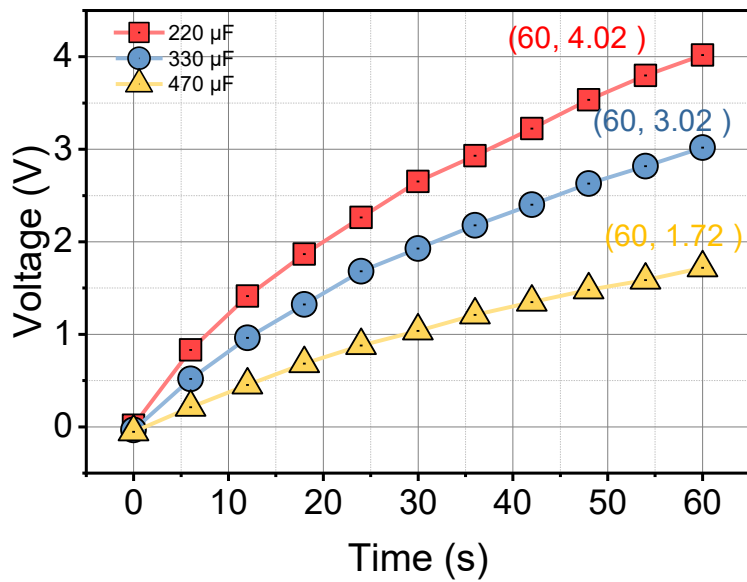


Figure S30: The charging histories of a single MO-TENG using PMM for different capacitors.

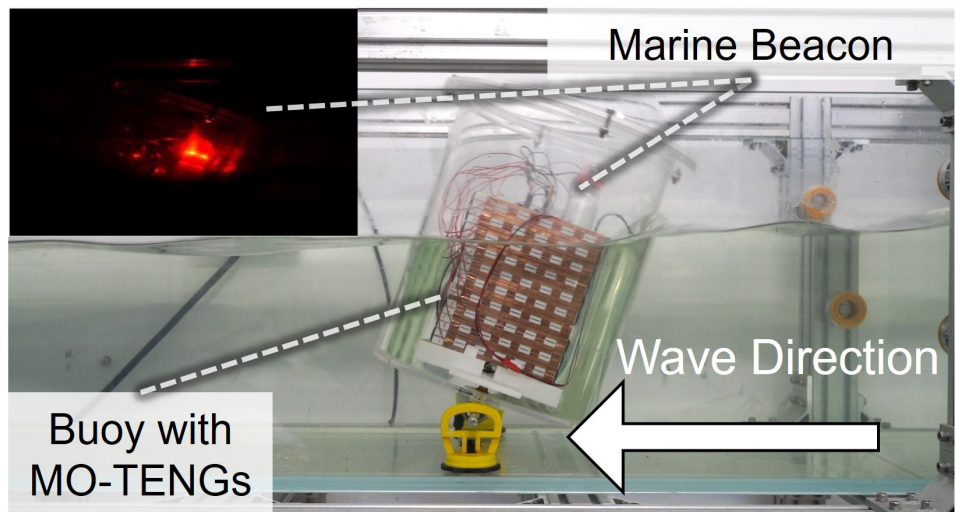


Figure S31: Powering marine navigation light with stacked MO-TENGs in the water tank.

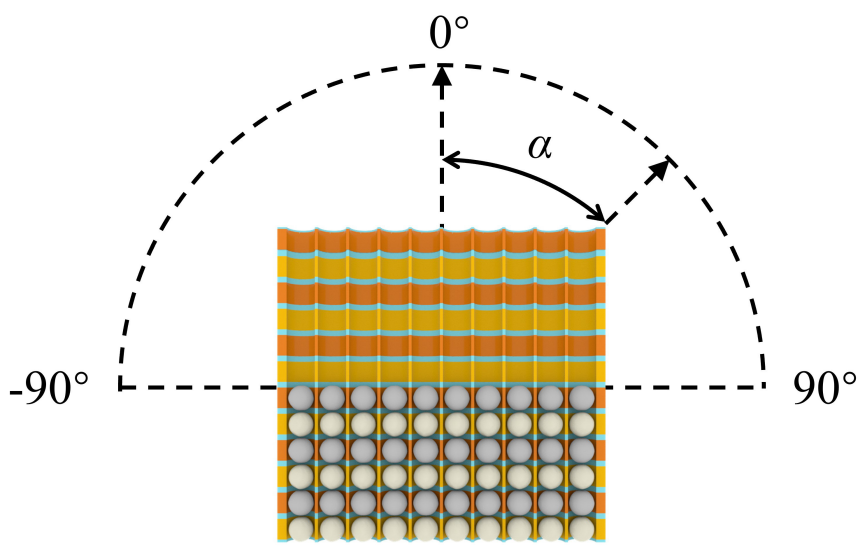


Figure S32: The schematic diagram of the angle α between the tunnel orientation and the wave direction.

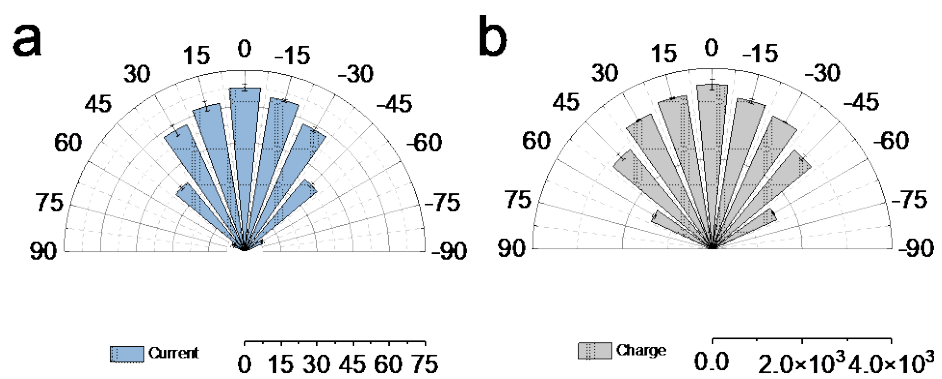


Figure S33: The current output and transfer charge of stacked 10 MO-TENG units with different α . Data are presented as mean values \pm SD.

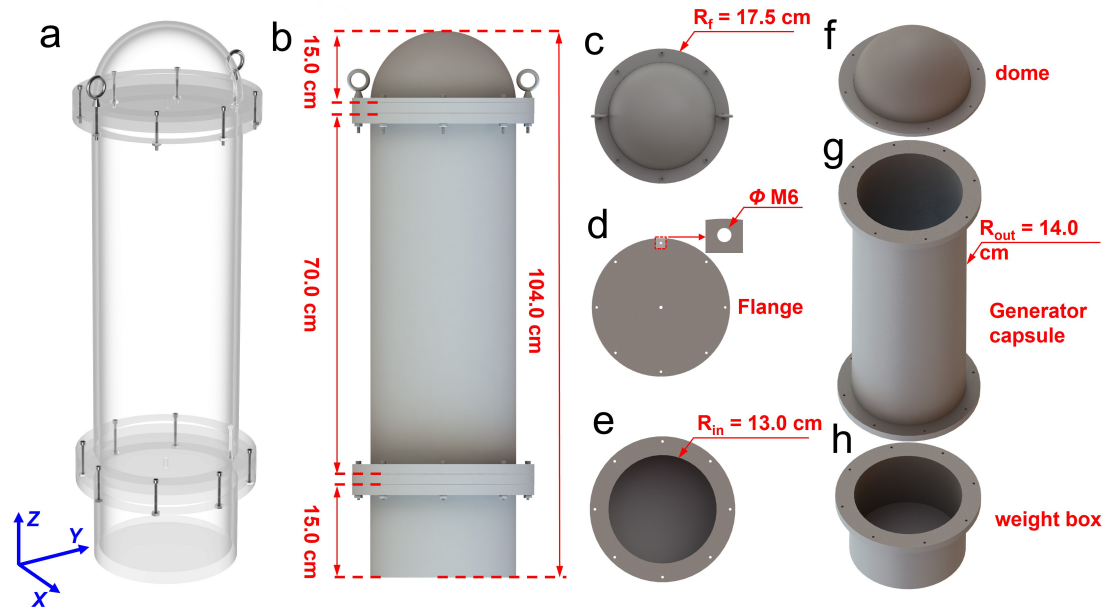


Figure S34: Dimension details of the acrylic buoy shown in [Figure 4h-i](#).



Figure S35: Photograph of the buoy stacked with 30 MO-TENG units.



Figure S36: Photograph of the random wave tank.

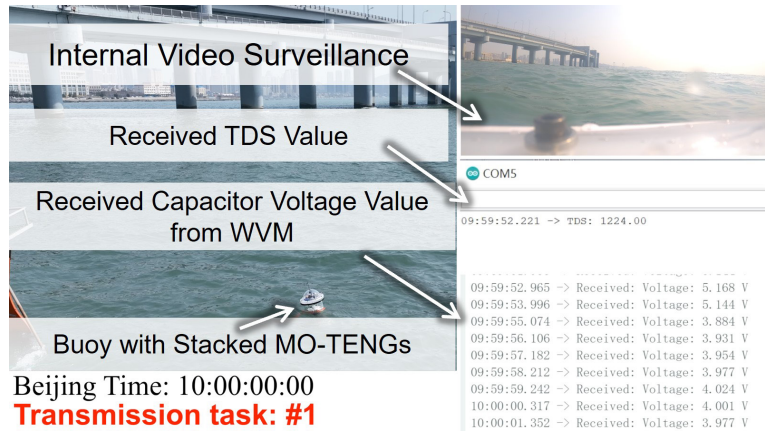


Figure S37: Photograph of the stacked MO-TENGs executing sensing tasks in the real ocean environment.

Table S1. Summary of previously reported TENGs for blue energy harvesting.

	Year	Name	Working Mode	Features	Typical Output				Volume (cm ³)	Application	Ref
					Q_{sc}	Power (mW)	Power Density (W/m ³ ·Hz)	Optimal Resistance			
1	2023	MO-TENG	Rolling Mode	Multi-tunnel; Grating Electrodes; Opposite Charge Enhancement	379.03 nC (Motor, 0.5 Hz)	Peak: 37.17 (Motor, 0.5 Hz, Per unit) RMS: 2.19 (Motor, 0.5 Hz, Per unit)	Peak: 185.4 (Motor, 0.5 Hz, Per unit) RMS: 10.92 (Motor, 0.5 Hz, Per unit)	200 MΩ (Motor, 1 Hz)	400.98	Navigation Light; Self-powered TDS Sensing; Self-powered LoRa Communication	This work
2	2023	SR-TENG	Rolling mode		810 nC (Motor, 2 Hz)	Peak: 16 (Motor, 2 Hz) RMS: 2.9 (Motor, 2 Hz) (ten units)	Peak: 26.435 (Motor, 2 Hz) RMS: 5.04 (Motor, 2 Hz) (ten units)	300 MΩ (Motor, 2 Hz)	302.63	LEDs; Temperature and Humidity Sensor;	[9]
3	2023	FE-TENG	Rolling mode	Bio-inspired	N/A	N/A	Peak: 5.6 (Motor, 1.25 Hz)	1000 MΩ (Motor, 1.25 Hz)	N/A	LEDs; Thermometer	[10]
4	2019	Self-assembly TENG	Rolling mode	Self-assembly	520 nC (Motor, 2 Hz, one unit)	Peak: 8.75 (Motor, 1.67 Hz)	Peak: 19.55 RMS: 5.20 (Motor, 1.67 Hz)	1000 MΩ (Motor, 1.67 Hz)	268	LEDs; Thermometer; Wireless transmitter;	[11]
5	2023	Chiral Network of Triboelectric Nanogenerator	Rolling mode	Chiral networks	540 nC (Motor, 1.5 Hz, Per Unit)	Peak: 7.88 (motor, 1.5 Hz) RMS: 2.18 (motor, 1.5 Hz)	Peak: 19.61 (motor, 1.5 Hz) RMS: 5.42 (motor, 1.5 Hz)	1000 MΩ (Motor, 1 Hz)	267.95	LEDs; T&H Sensing (Wireless)	[7]
6	2021	Spherical TENG	Rolling mode	Polacrylate Balls	820 nC (Motor, 5.9 Hz, one unit)	Peak: 10.7 (Motor, 5.9 Hz)	Peak: 3.47 (Motor, 5.9 Hz)	300 MΩ (Motor, 5.9 Hz)	527	LEDs; Timer	[12]

7	2019	T-TENG	Rolling mode	Tower-like	46 nC <u>(Motor, 1.2 Hz)</u> <u>(one unit)</u>	Peak: 0.143 <u>(Motor, 1.2 Hz)</u> <u>(one unit)</u> Peak: 14.734 <u>(Motor, 1.2 Hz)</u> <u>(ten units)</u>	Peak: 1.03 <u>(Motor, 1.2 Hz)</u> <u>(one unit)</u> Peak: 10.6 <u>(Motor, 1.2 Hz)</u> <u>(ten units)</u>	2000 MΩ <u>(Motor,</u> <u>1.2 Hz)</u> <u>(one unit)</u> 300 MΩ <u>(Motor,</u> <u>1.2 Hz)</u> <u>(ten units)</u>	1390	LEDs; Temperature Sensor	[13]
8	2021	S-TENG	Rolling mode	Sandwich-shape	600 nC <u>(Motor, 2 Hz)</u> <u>(one unit)</u>	Peak: 25.22 <u>(Motor, 2 Hz)</u> <u>(one unit)</u>	Peak: 17.325 <u>(Motor, 2 Hz)</u> <u>(one unit)</u>	500 MΩ (Motor, 2 Hz)	727.85	LEDs;	[14]
9	2022	S-TENG	Rolling mode	Multi-tunnel	14.715 μC <u>(Motor, 2 Hz, 48</u> <u>layers)</u>	N/A	Peak: 24.535 <u>(Motor, 2 Hz)</u>	300 MΩ (Motor, 2 Hz)	N/A	LEDS; PH Sensor; Salinity Sensor	[15]
10	2021	WT-TENG	Sliding Mode	Solid-liquid Electrification	47 nC (Motor, 1 Hz)	N/A	Peak: 13.1 <u>(Motor, 1 Hz)</u> RMS: 3.8 <u>(Motor, 1 Hz)</u>	Peak: 10 GΩ RMS: 4 GΩ (Motor, 1 Hz)	5.2	LEDs;	[1]
11	2020	CS-TENG	Contact- Separation	Charge Pumping	3.3 μC (Motor, 0.7 Hz)	Peak: 126.8 <u>(Motor, 1 Hz)</u> RMS: 1.4 <u>(Motor, 1 Hz)</u>	Peak: 17.81 <u>(Motor, 1 Hz)</u> RMS: 0.19 <u>(Motor, 1 Hz)</u>	517 kΩ (Motor, 0.7 Hz)	488.79	LEDs; Thermometer; Barometer	[2]
12	2019	OB-TENG	Contact- Separation	Multi-layer	10.5 μC (Motor, 1 Hz)	Peak: 38.7 <u>(Motor, 1 Hz)</u> RMS: 3.45 <u>(Motor, 1 Hz)</u>	Peak: 9.675 <u>(Motor, 1 Hz)</u> RMS: 0.863 <u>(Motor, 1 Hz)</u>	13.8 MΩ <u>(Motor, 1</u> <u>Hz)</u>	4000	LEDs; Thermometer;	[3]

13	2023	DE-TENG	Sliding Mode	Solid-liquid Electrification	0.55 μC (Motor, 0.5 Hz)	Peak: 0.85 <u>(Motor, 0.5 Hz)</u> RMS: 0.14 <u>(Motor, 0.5 Hz)</u>	Peak: 61.9 <u>(Motor, 0.5 Hz)</u> RMS: 9.88 <u>(Motor, 0.5 Hz)</u>	500 MΩ	27.3	LEDs; Thermometer; TDS sensing	[4]
14	2023	CS-TENG	Sliding Mode	Frequency Up-Conversion	1.1 μC (Motor, 1.75 Hz)	Peak: 14.36 (motor, 1.75 Hz) RMS: 3.53 (motor, 1.75 Hz)	Peak: 19.71 (motor, 1.75 Hz) RMS: 4.85 (motor, 1.75 Hz)	560 kΩ (Motor, 1.75 Hz)	416	LEDs; Thermometer; Anemometer	[5]
15	2019	TD-TENG	Sliding Mode	Eccentric Pendulum	3.3 μC (Motor, 1 Hz)	Peak: 29.4 <u>(Motor, 1 Hz)</u> RMS: 7 <u>(Motor, 1 Hz)</u>	Peak: 30.21 <u>(Motor, 1 Hz)</u> RMS: 7.19 <u>(Motor, 1 Hz)</u>	1 MΩ (Motor, 1 Hz)	973.3	LEDs; TDS Sensing	[6]
16	2023	WLM-TENG	Sliding Mode		1.1 μC (Wave, 1 Hz)	Peak: 50 <u>(Wave, 1 Hz)</u> RMS: 2.99 <u>(Wave, 1 Hz)</u>	Peak: 14.1 <u>(Wave, 1 Hz)</u> RMS: 0.84 <u>(Wave, 1 Hz)</u>	200 kΩ (Wave, 1 Hz)	3546.09	LEDs; Thermometer; Barometer; TDS sensing	[8]

Supplementary Notes

Supplementary Note 1. The diameter selection of dielectric balls and multi-tunnel grating electrodes

PTFE balls are commonly utilized in rolling mode TENGs due to their wide accessibility. Balls of different diameters have different weights. Contact force, as a key parameter in triboelectrification, is related to the weights of balls in rolling mode. To determine an appropriate diameter, transfer charge density was studied with various PTFE balls with different diameters. As presented in [Figure N1](#), we utilized five PTFE balls with different diameters ranging from 5 mm to 18 mm to prototype rolling mode TENGs with different dimensions. The housing of these TENGs was fabricated using a 3D printer, and then one pair of copper films was attached as electrodes. For a fair comparison, we let the width of the copper electrodes in this prototype match that of the PTFE balls, and the copper electrode length equals five diameters. Additionally, the gap between the two electrodes is uniformly set at 1 cm. The details can be found in [Figure N2](#). Here, we define the charge weight density to identify the impact of weight on the output and then help select the diameter of the ball. The charge weight density is calculated as $\frac{\text{the transfer charge (nC)}}{\text{weight of five PTFE balls (g)}}$. [Figure N3](#) depicts the dependence between the diameter of the balls used and the weight of five balls, the transfer charge output, and the charge weight density. As the diameter of the balls increases, both the weight of the five PTFE balls and the transfer charge output exhibit similar growth trends. Nonetheless, the charge weight density initially increases with the diameter and then stabilizes once the diameter reaches 12.7 mm. Therefore, the dielectric ball with a diameter of 12.7 mm was selected for subsequent experiments.

Furthermore, we examined the impact of the multi-tunnel grating electrodes' dimensions (tunnel diameter and electrode segments) on the performance of MO-TENGs. [Figure N4](#) presents the waveforms of the short current transfer charge (Q_{sc}) of MO-TENGs with different tunnel diameters and four electrode segments. Among the results in [Figure N4](#), TENG fabricated with a 13.5 mm tunnel diameter yields the best performance. There are two reasons behind this. First, the 13mm diameter tunnel is nearly the same as the 12.7mm diameter of the dielectric ball, potentially hindering the ball's rolling motion. Second, as the diameter of the tunnel increases further, the space between the electrode and the dielectric ball rises, which can diminish the effectiveness of electrostatic induction. [Figure N5](#) shows the I_{sc} output of the TENG with different electrode segments, and inserted photographs depict the corresponding prototype. With the electrode segments increasing from 4 to 14, I_{sc} rises from 0.15 μA to 1.57 μA . This result is attributed to two key factors: Firstly, increasing the number of segments extends the tunnel length, allowing it to accommodate more dielectric balls. Secondly, adding more electrode segments accelerates the charge transfer rate, thereby boosting the short-circuit current output. Therefore, the diameter of the dielectric ball and the

multi-tunnel are selected as 12.7 mm and 13.5 mm, respectively, for the subsequent experiments. For the segmentation of grating electrodes, it is beneficial to maximize the number of gratings, ensuring that the dimensions still allow for high integration and ease of fabrication.



Figure N1: Photograph of rolling mode TENGs fabricated using PTFE balls with different diameters.

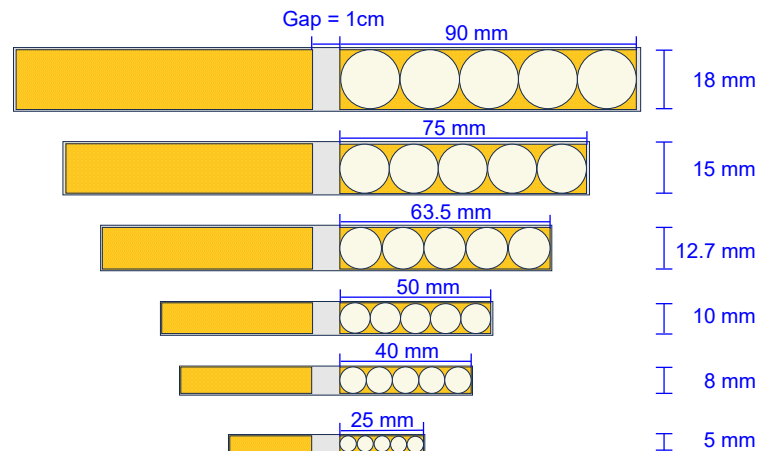


Figure N2: The parameter illustration of rolling mode TENGs fabricated using PTFE balls with different diameters.

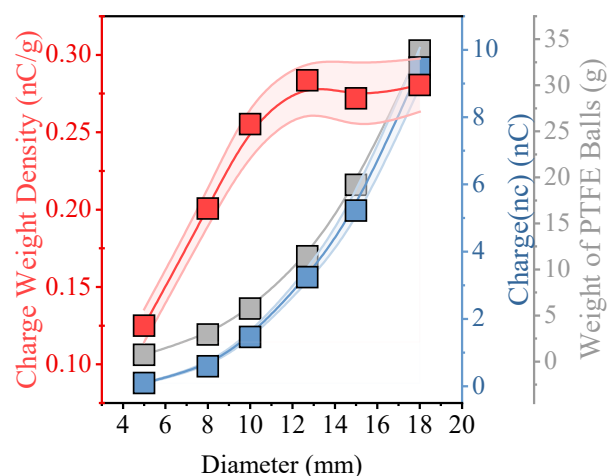


Figure N3: The weight, transfer charge, and charge weight densities of rolling mode TENGs using PTFE balls of various diameters. Data are presented as mean values \pm SD.

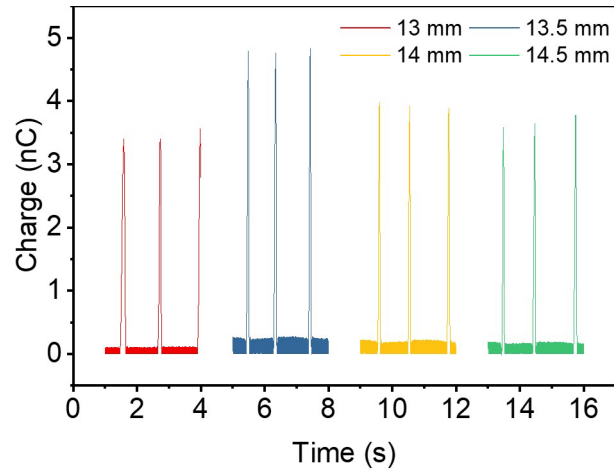


Figure N4: The transfer charge of rolling mode TENGs fabricated with one tunnel and 4 segment electrodes of various tunnel diameters.

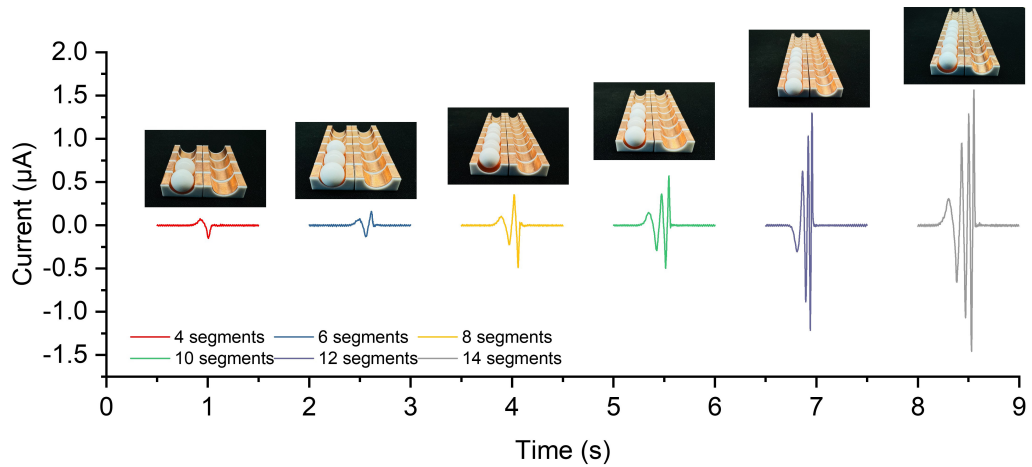


Figure N5: The current output of one tunnel grating electrode TENGs with different electrode segments.

Supplementary Note 2. The parameters of the designed buoy

The geometry of the carrier buoy is designed to be a revolving body so that it is isotropic (for various incident wave directions). First, we need to determine the diameter of the buoy. The frequency domain hydrodynamic response is calculated using ANSYS AQWA, and the pitch amplitude operator (RAO) is depicted in [Figure N6](#).

As the diameter varies from 0.2m to 0.8m (with the same draft and vertical center of gravity), we can find that the pitch RAO (pitch angle per 1 m incident wave amplitude) decreases with the diameter. This means we can select a relatively small diameter, as it will produce a desirable response and exhibit a relatively small displacement (as the displacement increases quadratically with the diameter). Considering the dimension of the TENG unit, the diameter is set to be 0.3 m. A small-scale buoy should weigh no more than 40 kg to facilitate deployment by manpower. Therefore, the draft is set to be 0.6m (displacement of 42.4 kg), and the freeboard is set to be 0.4m.

The influence of the vertical center of gravity (VCG) is also studied. In [Figure N7](#), the pitch RAO is compared when the VCG is set to 0.25 m and 0.2 m. It can be seen that a 5 cm increase in the VCG results in a roughly 20% rise in the pitch response. However, the metacentric height is 0.06 m when VCG is 0.25 m. As an important stability indicator, the metacentric height should not be too low to secure stability. Thus, the VCG is set to be 0.25 m.

Overall, the buoy is designed to be 1.0 m high with a diameter of 0.28 m.

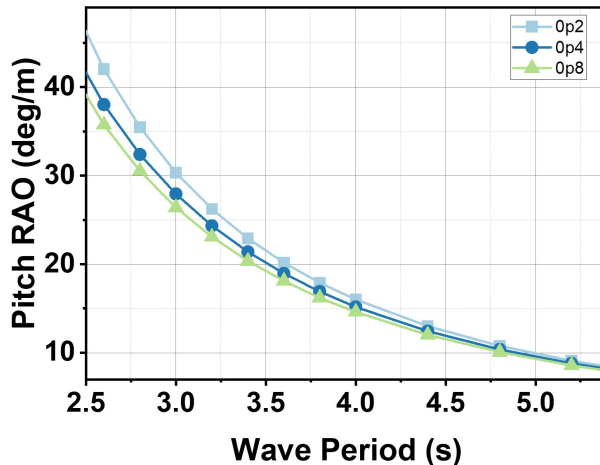


Figure N6: The selection of buoy diameter based on RAO.

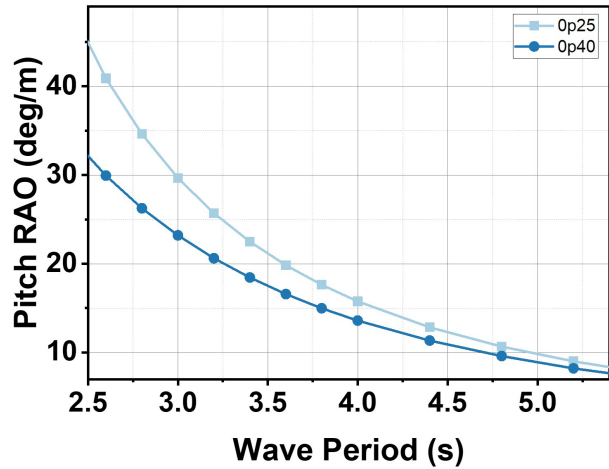


Figure N7: The selection of buoy vertical CoG based on RAO.

Supplementary Movie 1. MO-TENGs for lighting up LEDs.

Supplementary Movie 2. MO-TENGs for self-powered water quality sensing.

Supplementary Movie 3. MO-TENGs for powering marine navigation light.

Supplementary Movie 4. MO-TENGs enabled self-powered sensing under wave excitation.

Supplementary Movie 5. MO-TENGs enabled self-powered sensing in random wave tank.

Supplementary Movie 6. MO-TENGs enabled self-powered sensing in real ocean environment.

Reference

1. Wu, H., Wang, Z. & Zi, Y. Multi-Mode Water-Tube-Based Triboelectric Nanogenerator Designed for Low-Frequency Energy Harvesting with Ultrahigh Volumetric Charge Density. *Adv. Energy Mater.* **11**, 2100038 (2021).
2. Wang, H., Xu, L., Bai, Y. & Wang, Z. L. Pumping up the charge density of a triboelectric nanogenerator by charge-shuttling. *Nature Communications* **11**, 4203 (2020).
3. Zhong, W. *et al.* Open-book-like triboelectric nanogenerators based on low-frequency roll-swing oscillators for wave energy harvesting. *Nanoscale* **11**, 7199–7208 (2019).
4. Liang, X. *et al.* Liquid–Solid Triboelectric Nanogenerator Arrays Based on Dynamic Electric-Double-Layer for Harvesting Water Wave Energy. *Advanced Energy Materials* **13**, 2300571 (2023).
5. Qiu, H., Wang, H., Xu, L., Zheng, M. & Wang, Z. L. Brownian motor inspired monodirectional continuous spinning triboelectric nanogenerators for extracting energy from irregular gentle water waves. *Energy & Environmental Science* **16**, 473–483 (2023).
6. Bai, Y. *et al.* High-performance triboelectric nanogenerators for self-powered, in-situ and real-time water quality mapping. *Nano Energy* **66**, 104117 (2019).
7. Li, X. *et al.* Three-dimensional chiral networks of triboelectric nanogenerators inspired by metamaterial’s structure. *Energy & Environmental Science* **16**, 3040–3052 (2023).
8. Han, J., Liu, Y., Feng, Y., Jiang, T. & Wang, Z. L. Achieving a Large Driving Force on Triboelectric Nanogenerator by Wave-Driven Linkage Mechanism for Harvesting Blue Energy toward Marine Environment Monitoring. *Advanced Energy Materials* **13**, 2203219 (2023).
9. Duan, Y. *et al.* Scalable rolling-structured triboelectric nanogenerator with high power density for water wave energy harvesting toward marine environmental monitoring. *Nano Res.* **16**, 11646–11652 (2023).
10. Jing, Z. *et al.* 3D fully-enclosed triboelectric nanogenerator with bionic fish-like structure for harvesting hydrokinetic energy. *Nano Res.* **15**, 5098–5104 (2022).
11. Yang, X. *et al.* Macroscopic self-assembly network of encapsulated high-performance triboelectric nanogenerators for water wave energy harvesting. *Nano Energy* **60**, 404–412 (2019).
12. Yuan, Z. *et al.* Spherical Triboelectric Nanogenerator with Dense Point Contacts for Harvesting Multidirectional Water Wave and Vibration Energy. *ACS Energy Lett.* **6**, 2809–2816 (2021).
13. Xu, M. *et al.* High Power Density Tower-like Triboelectric Nanogenerator for Harvesting Arbitrary Directional Water Wave Energy. *ACS Nano* **13**, 1932 (2019).
14. Wang, H. *et al.* Sandwich-like triboelectric nanogenerators integrated self-powered buoy for navigation safety. *Nano Energy* **84**, 105920 (2021).

15. Wang, H. *et al.* A Stackable Triboelectric Nanogenerator for Wave-Driven Marine Buoys. *Nanomaterials* **12**, 594 (2022).